Convection Initiation Aided by Lake-Breeze Convergence over the Niagara Peninsula

CHUN-CHIH WANG AND DANIEL J. KIRSHBAUM

Department of Atmospheric and Oceanic Sciences, McGill University, Montreal, Quebec, Canada

DAVID M. L. SILLS[a]

Environment and Climate Change Canada, Toronto, Ontario, Canada

(Manuscript received 24 April 2019, in final form 13 August 2019)

ABSTRACT

Observations from the 2015 Environment and Climate Change Canada Pan/Parapan American Science Showcase (ECPASS) and real-case, cloud-resolving numerical simulations with the Weather Research and Forecasting (WRF) Model are used to investigate two cases of moist convection forced by lake-breeze convergence over southern Ontario (18 July and 15 August 2015). The two cases shared several characteristics, including high pressure conditions, similar morning soundings, and isolated afternoon convection along a line of lake-breeze convergence between Lakes Erie and Ontario. However, the convection was significantly stronger in the August case, with robustly deeper clouds and larger radar reflectivities than in the July case. Synoptic and mesoscale analyses of these events reveal that the key difference between them was their large-scale forcing. The July event exhibited a combination of strong warm advection and large-scale descent at midlevels (850–650 hPa), which created an inversion layer that capped cloud tops at 4–6 km. The August case exhibited similar features (large-scale descent and warm advection), but these were focused at higher levels (700–400 hPa) and weaker. As a consequence, the convection in the August case was less suppressed at midlevels and ascended deeper (reaching over 8 km). Although the subcloud updraft along the lake-breeze convergence zone was also found to be stronger in the August case, this difference was found to be an effect, rather than a cause, of stronger moist convection within the cloud layer.

1. Introduction

The Great Lakes profoundly influence the weather and climate of nearby regions. Although they are arguably best known for lake-effect snow during winter (Peace and Sykes 1966; Niziol 1987; Reinking et al. 1993; Kristovich et al. 2017), they also generate numerous other phenomena including summertime lake breezes (e.g., Shenfeld and Thompson 1962; Moroz 1967; Lyons 1972; Estoque and Lai 1976). The latter are similar to sea breezes, in which a land–water temperature contrast drives a current of onshore flow during the daytime. At the leading edge of this onshore flow is the lake-breeze front (LBF), where vigorous updrafts result from frontogenesis and the undercutting of warmer land air by cooler lake air. These breezes are meteorologically important for several reasons, including their impacts on air pollution transport (e.g., Lyons and Cole 1973; Keen and Lyons 1978; Wentworth et al. 2015) and their initiation of moist convection and severe weather (e.g., Shenfeld and Thompson 1962; Leduc et al. 1993; King 1996; King et al. 2003), the latter of which is the focus of this study.

Southern Ontario, which borders three of the five Great Lakes (Ontario, Huron, and Erie) and contains many smaller lakes, is regularly affected by lake breezes (Comer and McKendry 1993; Sills 1998; Sills et al. 2011). It thus serves as a natural laboratory for studying the physics and meteorology of these breezes. Observational and numerical studies dating back several decades suggest that the onshore flows of southern Ontario lake breezes typically reach depths of 100–1000 m, with inland penetration from tens to hundreds of kilometers (e.g., Estoque and Lai 1976; Estoque and Gross 1981; Comer and McKendry 1993; Sills et al. 2011).

More recent insights into these breezes have been gained through field campaigns such as Southern Ontario

---

[a] Current affiliation: Department of Civil and Environmental Engineering, University of Western Ontario, London, Ontario, Canada.

Corresponding author: Chun-Chih Wang, chun-chih.wang@mail.mcgill.ca

DOI: 10.1175/MWR-D-19-0123.1

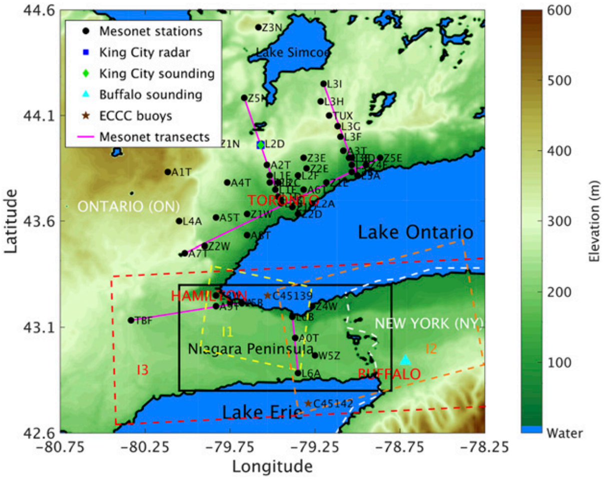

FIG. 1. The ECPASS field campaign setup. Colored contours indicate the terrain profile. The areal coverage of interpolation grids used for simulated LBF analysis are denoted by dashed boxes.

Oxidant Study-Meteorological Measurements (SOMOS; Sills and Salmon 1994; Sills 1998), Effects of Lake Breezes on Weather (ELBOW; Sills 1998; King et al. 1999; Sills et al. 2002; Alexander 2012; Alexander et al. 2018), and Border Air Quality and Meteorology Study (BAQS-Met; Levy et al. 2010; Makar et al. 2010; Hayden et al. 2011; Sills et al. 2011; Brook et al. 2013), which have used surface mesonets and aircraft to track the propagation of lake-breeze fronts and examine the resulting meteorological effects. One robust finding from these studies is that collisions between different lake-breeze fronts, or between lake-breeze fronts and other mesoscale boundaries, often favor the development of summertime deep convection. This result is consistent with studies of other similar mesoscale boundaries, in that storms tend to form or intensify when two such boundaries collide (e.g., Purdom 1976; Wilson and Schreiber 1986; Carbone et al. 1990, 2000). Using numerical simulations, Crook (1997) found that the collision of sea-breeze fronts over the narrow (50 km wide) Tiwi Islands frequently initiates or strengthens deep convection. This effect can be explained by the enhanced low-level convergence along the collision zone and/or the more balanced low-level horizontal vorticity across the collision boundary, which leads to more intense and erect updrafts (e.g., Mahoney 1988; Rotunno et al. 1988).

Given the importance of lake-breeze-forced convection in southern Ontario, a thorough understanding of the underlying processes is merited. Of particular relevance are the parameters regulating LBF frontogenesis and propagation, which ultimately control the occurrence of LBF collision and the strength of resulting subcloud updrafts, along with the multiscale factors governing the timing, duration, and intensity of the resulting convection. Because LBFs and their associated convection occupy very small scales (hundreds to thousands of meters), they may not be well represented in modern numerical weather prediction (NWP) models with $O(1)$ km grid spacings. Thus, an improved understanding of these processes may serve to benefit operational forecasting of such events.

In summer 2015, Environment and Climate Change Canada (ECCC) conducted a field experiment called the Environment Canada Pan/Parapan Am Science Showcase (ECPASS) over the ‘‘Greater Golden Horseshoe’’ (GGH) area of southern Ontario (Joe et al. 2018). This area includes the densely populated and economically developed regions from Lake Simcoe southward to the western tip of Lake Ontario, and from there eastward covering the entire Niagara Peninsula (Fig. 1). The primary mission of ECPASS was to enhance the weather monitoring and forecasting during the 2015 Toronto Pan and Parapan American Games (10–26 July and 7–15 August, respectively), which held events at several regional sporting venues.

The ECPASS observations, which included a surface mesonet, scanning Doppler lidars, and special radiosondes, provide another opportunity to advance the understanding of southern Ontario lake breezes. Mariani et al. (2018) used these observations to characterize the three-dimensional structures of lake breezes in two ECPASS cases, and Dehghan et al. (2018) used them to evaluate the performance of a high-resolution NWP model in predicting lake-breeze characteristics under differing background winds. Importantly, Dehghan et al. (2018) found a general improvement in the model representation of lake breezes when the model horizontal grid spacing was decreased from 2.5 to 0.25 km, consistent with the findings of Leroyer et al. (2014). These findings, which are to be expected given the narrowness of the LBFs themselves (~1 km; Chiba 1993; Wood et al. 1999; Samiro 2015), suggest that subkilometer grid spacings may be required to properly simulate lake breezes.

As mentioned above, previous lake-breeze studies over southwestern Ontario (about 100–200 km west of the ECPASS study region) have identified several cases of convective precipitation forced by colliding LBFs. To the authors’ knowledge, there has not been any detailed analysis of this mechanism over the GGH. However, given the short distances between the quasi-parallel coastlines of Lakes Ontario and Erie over the Niagara Peninsula (Fig. 1), this area may be a potential hotspot for the collision of LBFs and attendant moist convection. Therefore, this article investigates the dynamics and sensitivities of lake-breeze-forced moist convection over the GGH, using the ECPASS observations in conjunction with high-resolution, cloud-resolving numerical simulations. The ECPASS observational datasets are summarized in section 2. Section 3 describes the observed evolution of the lake breezes and associated moist convection during two selected cases, chosen for their similar large-scale conditions but different cumulus development. The numerical setup is described in section 4 and the simulated lake breezes and associated moist convection are summarized and compared to the ECPASS observations in section 5. Section 6 compares the large-scale and lake-breeze forcing of moist convection during the two cases. The conclusions are presented in section 7.

2. ECPASS datasets

a. The mesonet

During ECPASS, a ground-based, mesoscale observational network (mesonet) comprising 40 compact surface weather stations (25 Vaisala WXT520 and 15 Lufft WS600/60), 10 Automated Transportable Meteorological Observing Stations (ATMOS), and three standard ECCC automated weather stations (Auto8) was deployed in the Greater Golden Horseshoe Region (Fig. 1). All stations reported temperature T, dewpoint T_d, winds, and pressure p every minute, with basic quality control to remove outlying values. Most stations were installed in transects perpendicular to the shores of Lakes Ontario and Erie, permitting close monitoring of daytime lake-breeze evolution. In total, 20 of the 53 total surface stations were positioned on rooftops less than two stories high, mostly in urban areas where ground-level sites were unavailable. The winds at these stations may have experienced some urban canyon effects induced by the surrounding structures. Nevertheless, to maximize the amount of data available, we have chosen to retain the rooftop measurements in our analysis. Other weather monitoring platforms such as research buoys, Doppler lidars, ultraviolet (UV) stations, air quality stations, and lightning detection networks were also utilized during the field campaign (not shown). For a detailed description of this mesonet, see Joe et al. (2018).

b. Operational buoys

In addition to the ECPASS research buoys (not shown), ECCC also operates two buoys in the vicinity of the Niagara Peninsula (Fig. 1). One of these buoys is located over Lake Ontario (C45139) and the other over Lake Erie (C45142). These buoys report wave conditions, winds, air temperature, and lake surface temperature every hour.

c. Radar

ECCC operates a dual-polarized, 5625 MHz, 5-cm C-band weather radar at King City, Ontario, Canada (Fig. 1), that volumetrically scans over 20 elevation angles. The radar has a maximum range of 250 km and scans in 10-min cycles (Hudak et al. 2006; Boodoo et al. 2010). Along with precipitation, mesoscale boundaries like lake-breeze fronts and outflow boundaries can sometimes be detected as reflectivity ''fine lines.'' Such signals are thought to arise from wind convergence along these boundaries concentrating small airborne objects (e.g., dust, birds, and insects), which return weak echoes in clear air (Wilson and Schreiber 1986; Wilson et al. 1994).

For the radar analysis contained herein, several steps were taken to filter out nonmeteorological signals, including (i) data points with copolar correlation coefficient $\rho_{co} < 0.80$ were masked, since hydrometeors tend to have ρ_{co} values closer to 1 (Fabry 2015), (ii) points with differential reflectivity $Z_{dr} < -0.25$ or $Z_{dr} > 6$ were removed, since they indicate noise and/or insect echoes, and (iii) the difference between echo top and echo bottom, which are defined by the lowest and highest altitudes where the radar reflectivity exceeds 0 dBZ, must exceed 500 m. Beyond these measures, manual masking is performed to remove any residual (obvious) noise.

d. Soundings

To monitor upper-air conditions, a special balloon sounding was launched at King City up to four times a day (Fig. 1). Also, the U.S. National Weather Service launched twice-daily operational balloon soundings from Buffalo, New York (Fig. 1).

e. Observational LBF tracking

Using the Aurora workstation (Greaves et al. 2001), the ECPASS Research Support Desks (RSDs) overlaid the radar, visible satellite, and mesonet observations and visually detected LBFs and other mesoscale boundaries according to the criteria listed in Table 1 of Sills et al. (2011). Such criteria include the presence of cumulus cloud lines or sharp clearing of clouds behind the LBF (Segal et al. 1997), radar reflectivity fine lines, and rapid wind shifts to the onshore direction over a short horizontal distance behind the front. Errors in the analyzed boundary positions are as large as ±10 km if only low-density surface observations are used for identification but decrease to as little as ±1 km when high-density surface observations (e.g., mesonet)

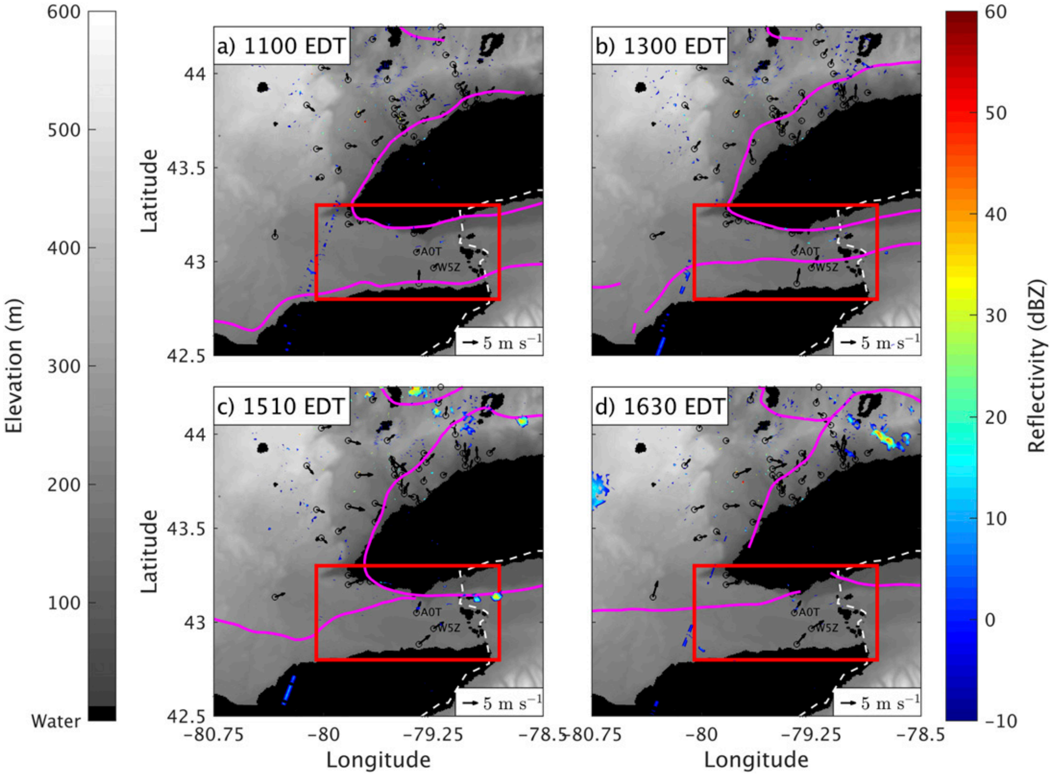

FIG. 2. Observed radar reflectivity (color shading), surface mesonet wind observations (arrows), and analyzed positions of LBFs (purple lines) based on the ECPASS observations on 18 Jul 2015 at (a) 1100, (b) 1300, (c) 1510, and (d) 1630 EDT. The terrain profile is plotted in gray shading. The red box indicates the Niagara Peninsula where the maximum radar reflectivity and echo-top height are computed.

and other datasets such as satellite and radar observations are incorporated (Sills et al. 2011).

Real-time boundary analyses were performed during the Games at the RSDs, though not every day and not for every hour. In addition, all data were not always available in real time. After the Games, a complete boundary analysis dataset was created using the RSD tools covering every hour of every day during the ECPASS period after incorporating any missing observations. The preliminary, real-time LBF positions were used as a ''first guess'' when available and revised as necessary based on the updated observations.

Many of the days analyzed featured widespread deep moist convection triggered by some combination of lake breezes and other meteorological boundaries (e.g., synoptic fronts and storm outflow boundaries). In the present study, we wish to isolate the influence of converging lake breezes on convection initiation in nominally high pressure environments with minimal preexisting precipitation. From the list of ECPASS mesoanalysis days, we identified only two cases, 18 July and 15 August, where isolated convective precipitation was locally triggered by the convergence of Lakes Ontario and Erie breezes over the Niagara Peninsula. Although this convection was not particularly deep or intense (no lightning or severe weather was reported), the simplicity of these cases facilitates the understanding of lake-breeze collisions and their impacts on cloud formation, in the absence of other complicating factors. The insights provided herein may be useful for interpreting more intense convection events driven by similar boundary layer mechanisms.

3. Case studies

a. Overview

1) 18 JULY

Both Lakes Ontario and Erie generated lake breezes in this case, with LBFs forming along the western shores of Lake Ontario and northern shores of Lake Erie by 1100 eastern daylight time (EDT, Fig. 2a). A lake breeze also formed to the south of Lake Simcoe. Because the target region in this study is the Niagara Peninsula, we focus exclusively on lake breezes and precipitation over that region in both cases. The air temperature over the

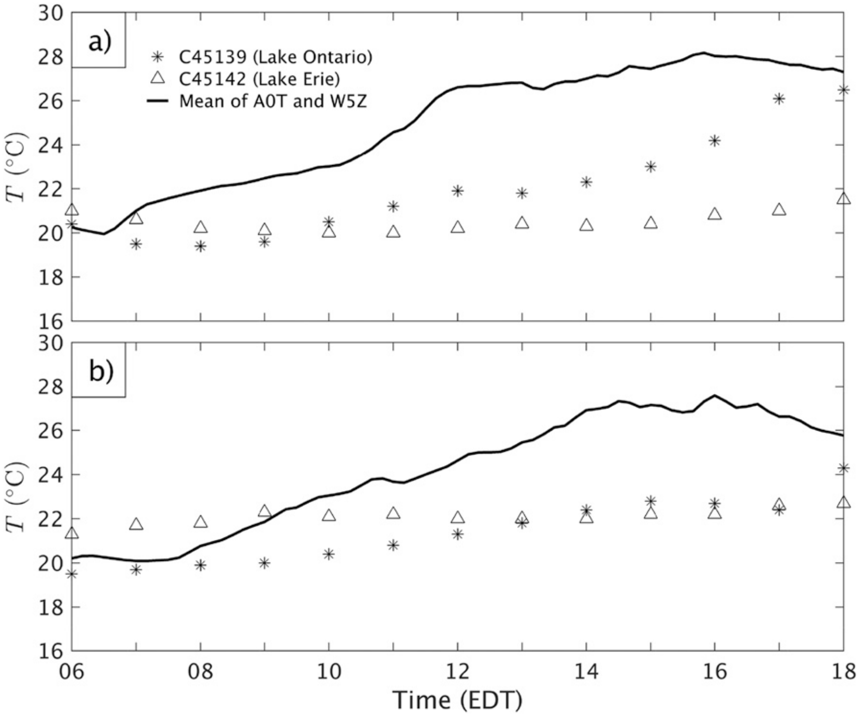

FIG. 3. Time series of observed air temperature at ECCC buoys C45139 and C45142 and averaged observed air temperature at mesonet stations A0T and W5Z on (a) 18 Jul and (b) 15 Aug 2015.

interior of the Niagara Peninsula (taken as the mean at mesonet stations A0T and W5Z) was 4°–5°C warmer than those over Lakes Ontario and Erie (at Buoys C45139 and C45142, respectively) at this time (Fig. 3a). By 1300 EDT, the northern Lake Ontario LBF had propagated 10–15 km inland while the southern part stayed locked to the shoreline (Fig. 2b). This difference in propagation is likely owing to the moderate southwesterly background flow ($6\,\mathrm{m\,s^{-1}}$ at a meteorological wind direction of 240°, based on the averaged 950–850-hPa flow at 1300 EDT 18 July 2015 King City special sounding). This flow parallels the northern LBF, allowing it to propagate onshore, but opposes the southern LBF. Like the northern Lake Ontario LBF, the northern Lake Erie LBF also reached 15–20 km inland by this time. Behind this LBF, no obvious wind direction shift was found due to the onshore component of the ambient winds, but a clear increase in wind speed was apparent.

Two hours later, the northern Lake Erie LBF had propagated farther inland and collided with the southern Lake Ontario LBF (Fig. 2c). The two LBFs actually collided at around 1430 EDT, but we show 1510 EDT instead because it indicates the first precipitation occurrence associated with the LBF collision. The majority of showers associated with this collision were concentrated along the resulting ''merged'' boundary (consistent with the definition in Alexander et al. (2018), where two boundaries combine to form a single boundary/updraft zone). The maximum radar reflectivity, computed at the lowest scanning angle of 0.5°, was ~35 dBZ and the maximum echo-top height reached close to 6 km above mean sea level (MSL; Figs. 4a,b). Scattered showers also developed between Lake Simcoe and Lake Ontario as their LBFs propagated inland.

The showers over the Niagara Peninsula only lasted about an hour. By 1600 EDT, the peninsula was again precipitation free (Fig. 4a). The merged boundary continued to propagate northward toward Lake Ontario under the moderate southwesterly background flow. A segment of this merged boundary actually moved over Lake Ontario by this time, which appears as a discontinuity in the merged LBF (Fig. 2d). The northern branch of the Lake Ontario LBF can also be seen interacting with the Lake Simcoe LBF to produce additional showers northeast of Toronto.

2) 15 AUGUST

The LBFs in this case began to form along the western shores of Lake Ontario and northern shores of Lake Erie around noon, about an hour later than in the July case (cf. Figs. 5a and 2a). In this case, the air temperature

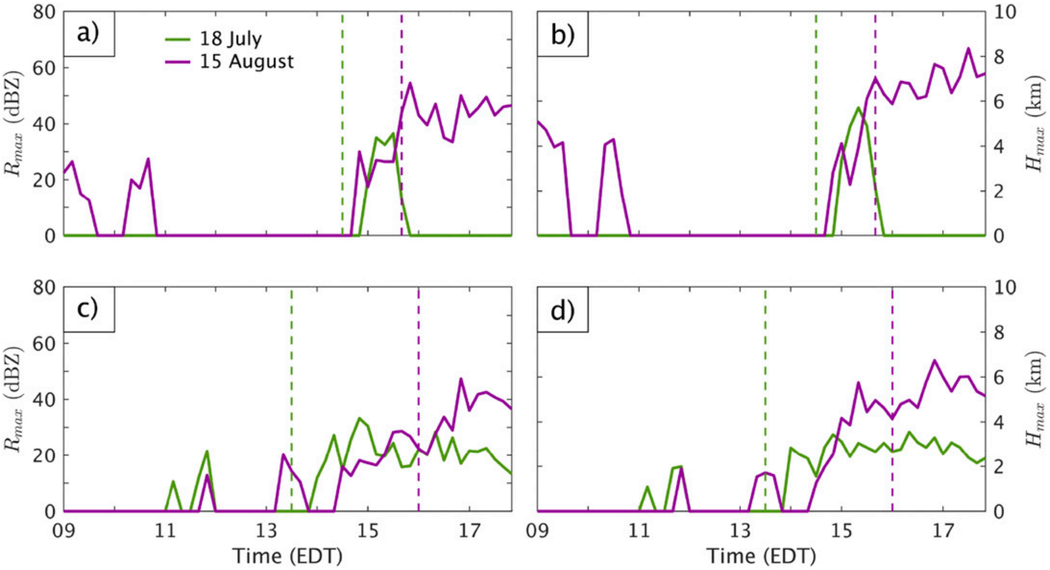

FIG. 4. Time series of (a),(b) observed and (c),(d) simulated (left) maximum radar reflectivity ($R_{\max}$) and (right) echo-top height ($H_{\max}$) over the Niagara Peninsula (the boxed region in Figs. 2 and 5). The times of LBF collision are indicated by dashed lines.

contrasts between the interior of the peninsula and the lakes did not reach the same magnitude as those during the lake-breeze formation in the July case (~4°C) until 1300 EDT (Fig. 3b), which could partly explain the later formation of the lake breezes on this day. Similar to the July case, the Pan Am study area was precipitation free at the time of LBF formation. However, some lingering precipitation associated with a departing disturbance was apparent before 1030 EDT (Fig. 4a).

By 1400 EDT, both the Lake Ontario and Lake Erie LBFs had propagated noticeably inland (Fig. 5b), in contrast to the July case where only the latter did so. Although no King City special soundings were available at this time (the only special sounding available was taken at 0400 EDT), this more symmetric inland propagation of the two LBFs suggests a weaker background flow than that in the July case. Over the Niagara Peninsula, the southern Lake Ontario LBF and the northern Lake Erie LBF gradually approached each other. The winds behind these LBFs switched to onshore while the winds in between them were light and variable.

The southern Lake Ontario LBF collided with the northern Lake Erie LBF at around or just prior to 1600 EDT (Fig. 5c). Some isolated showers formed over the peninsula prior to the frontal collision (Fig. 4a), possibly due to the relatively weak convective inhibition in this case (as will be shown later). After LBF collision, more widespread and stronger storms developed along the merged boundary due to enhanced convergence there. The strongest cell at this time was located near the eastern edge of the Niagara Peninsula, with a maximum radar reflectivity reaching ~55 dBZ and a maximum echo top around 6 km MSL (Figs. 4a,b).

Unlike the showers triggered along the merged LBF in the July case, which only lasted briefly, storms developed continuously along the merged boundary in this case (Fig. 5d). The quasi-stationary nature of the merged boundary also contrasted with that in the July case, where it moved northward steadily under a southwesterly background flow. The late-afternoon storms had radar reflectivities up to ~50 dBZ and their maximum echo top reached beyond 8 km MSL (Figs. 4a,b).

Comparing the two cases, the moist convection initiated by the collision of Lake Ontario and Lake Erie LBFs in the August case was stronger than that in the July case. The question that motivates the remainder of this study is: What led to this difference in the convection intensity? Was the large-scale environment more favorable in the August case, or did its LBFs provide stronger subcloud lifting for moist convection initiation?

b. *Large-scale conditions*

The 6-hourly, 12-km horizontal resolution North American Mesoscale Forecast System (NAM) analyses are used to represent the synoptic weather pattern. This analysis provides a 3D estimate of the meso- to synoptic-scale flow at 39 pressure levels from 1000 to 50 hPa in 25-hPa intervals. For brevity, we focus on just the 1800 UTC (1400 EDT) analysis, which best represents the large-scale flow just before the active convection period.

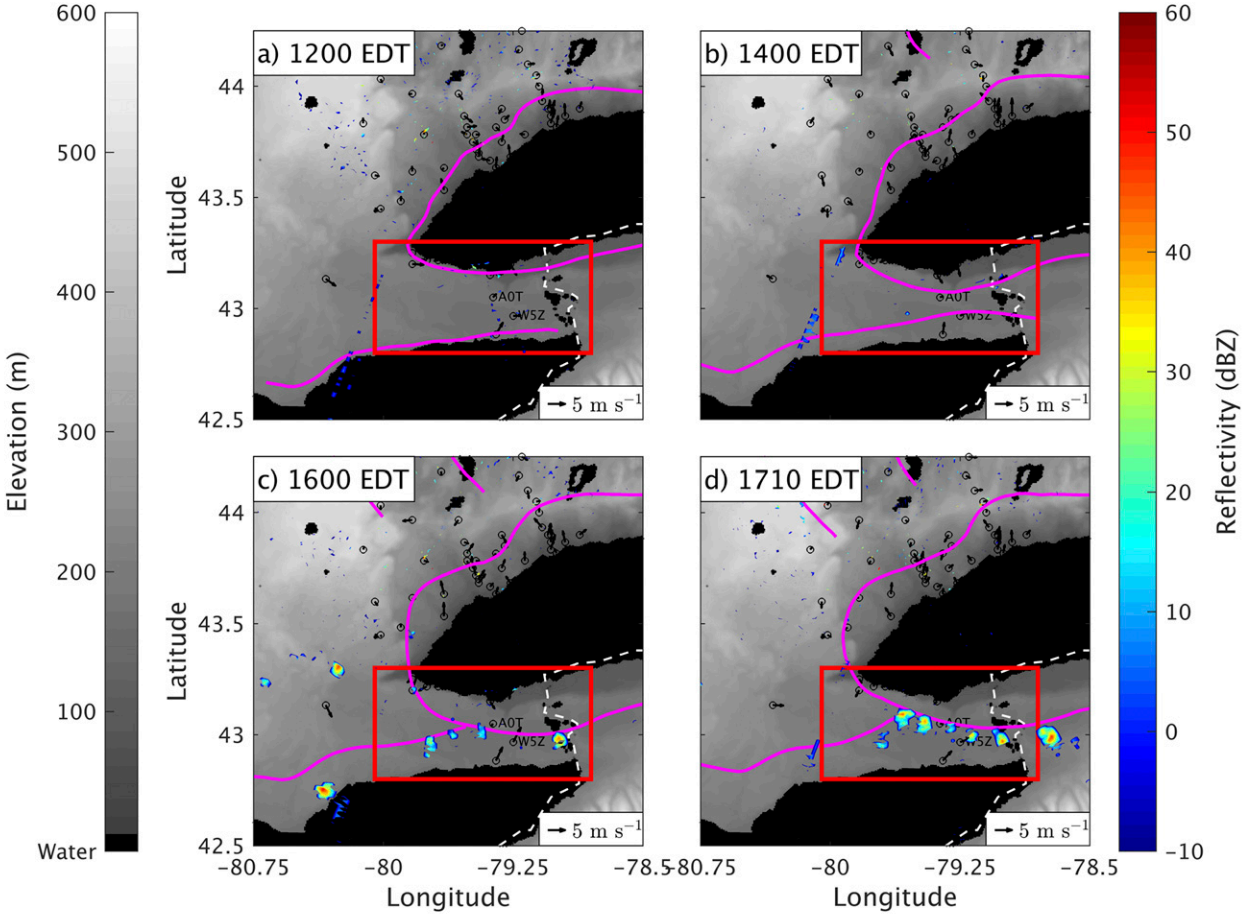

FIG. 5. As in Fig. 2, but for 15 Aug 2015 at (a) 1200, (b) 1400, (c) 1600, and (d) 1710 EDT.

1) 18 JULY

In this case, a 500-hPa ridge was building over the Pan Am study area (Fig. 6a). Weak negative relative vorticity advection was consequently occurring over southern Ontario, suggesting large-scale forcing for descent. Two short-wave troughs, one to the east and another to the west of the 500-hPa ridge, caused locally positive vorticity advection. These systems, however, were likely irrelevant to the flow conditions over the ECPASS study area.

Similar to the 500-hPa level flow pattern, a ridge prevailed across southern Ontario at 700 hPa (Fig. 6c). A tongue of warm air extending across the central Great Lakes was advected eastward by westerly winds. This advection partly contributed to the large increase (~5°C) in T at 700 hPa, as seen from the 0800 EDT and 2000 EDT Buffalo soundings (Fig. 7a), implying a gradual increase in the low- to midlevel static stability. Strong drying over 900–700 hPa and some moistening over 700–500 hPa were also observed.

The upper-level ridge was associated with surface high pressure over the southeastern United States. Anticyclonic flow around this high brought warm and moist air into the ECPASS study region (Fig. 6e). The surface equivalent potential temperature (θ_e) in this area reached a maximum of around 350 K. A light to moderate (2.5 m s^{-1}) southwesterly (230°) surface wind locally prevailed.

2) 15 AUGUST

This case also featured a 500-hPa ridge to the northwest of the ECPASS study region (Fig. 6b). A lingering 500-hPa short-wave trough was also situated just to the southeast. This setup led to strong negative vorticity advection aloft across the Pan Am study region. Consequent large-scale descent is suggested by the 0800 EDT and 2000 EDT Buffalo soundings, where a moderate (~3°C) increase in T and reduction in T_d occurred over the 750–350-hPa layer in the intervening 12-h period (Fig. 7b). No significant change in the low- to midlevel (900–700 hPa) T_d was observed.

As in the 18 July case, the flow around the 700-hPa ridge to the northwest of southern Ontario also advected

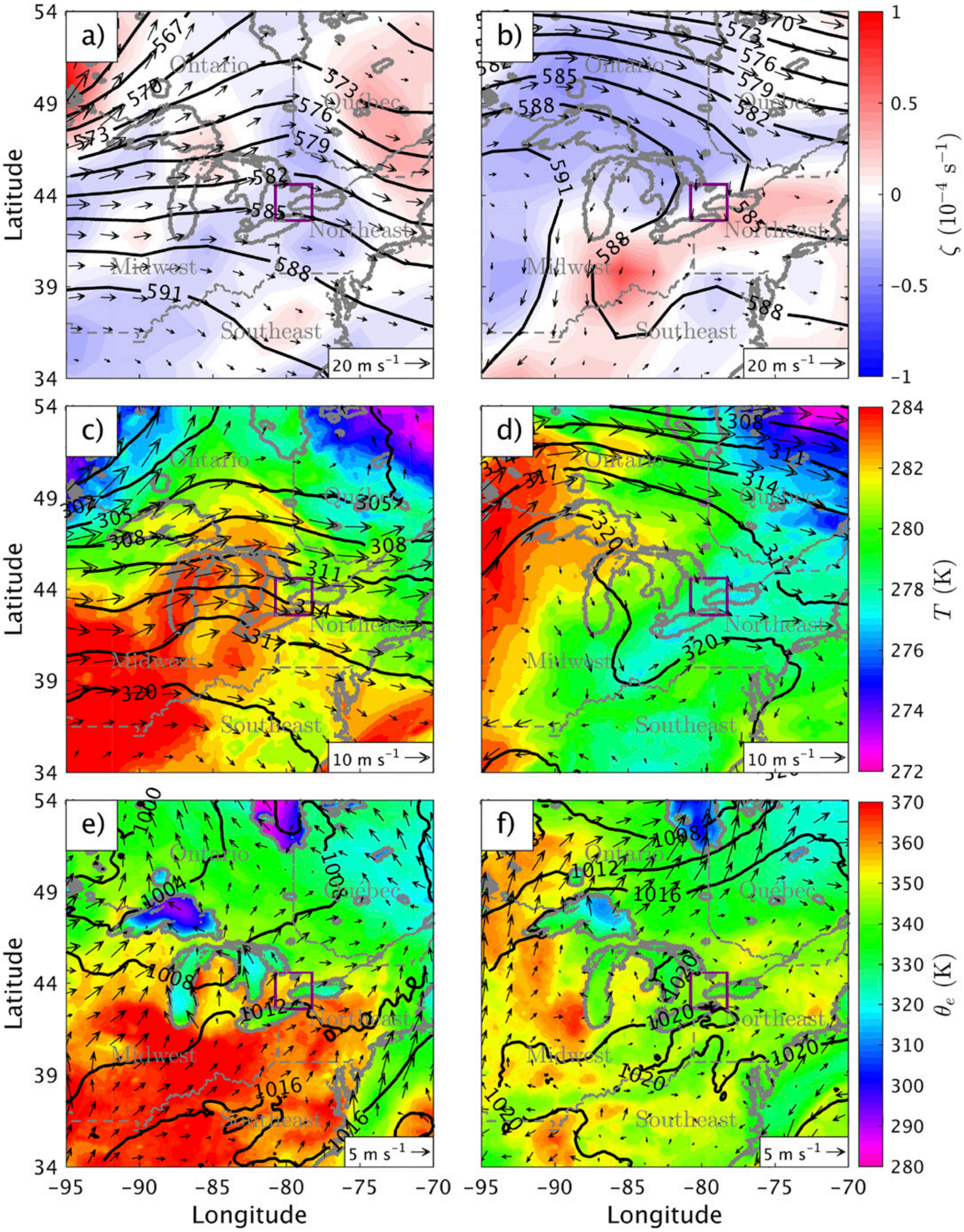

FIG. 6. Maps of (a) 500-hPa geopotential height (contours), relative vorticity (color shading), and geostrophic winds, (c) 700-hPa geopotential height (contours), temperature (color shading), and geostrophic winds, and (e) mean sea level pressure (contours), surface θ_e (color shading), and winds at 1800 UTC (1400 EDT) 18 Jul 2015. (b),(d),(f) As in (a),(c),(e), but for 1800 UTC (1400 EDT) 15 Aug 2015. The ECPASS study region is indicated by a purple box near the center of each panel.

relatively warm air into the Pan Am study region (Figs. 6d and 7b). However, the temperature gradients and wind speeds aloft were much weaker in this case, suggesting much weaker horizontal warm advection. Similar to the July case, a surface high pressure was located over the Southeast region of the United States (Fig. 6f). The mean surface wind across the ECPASS study region was weaker than that in the July case (1.5 vs 2.5 m s^{-1}) and was blowing from 250°. This weaker wind partly contributed to the more even propagation

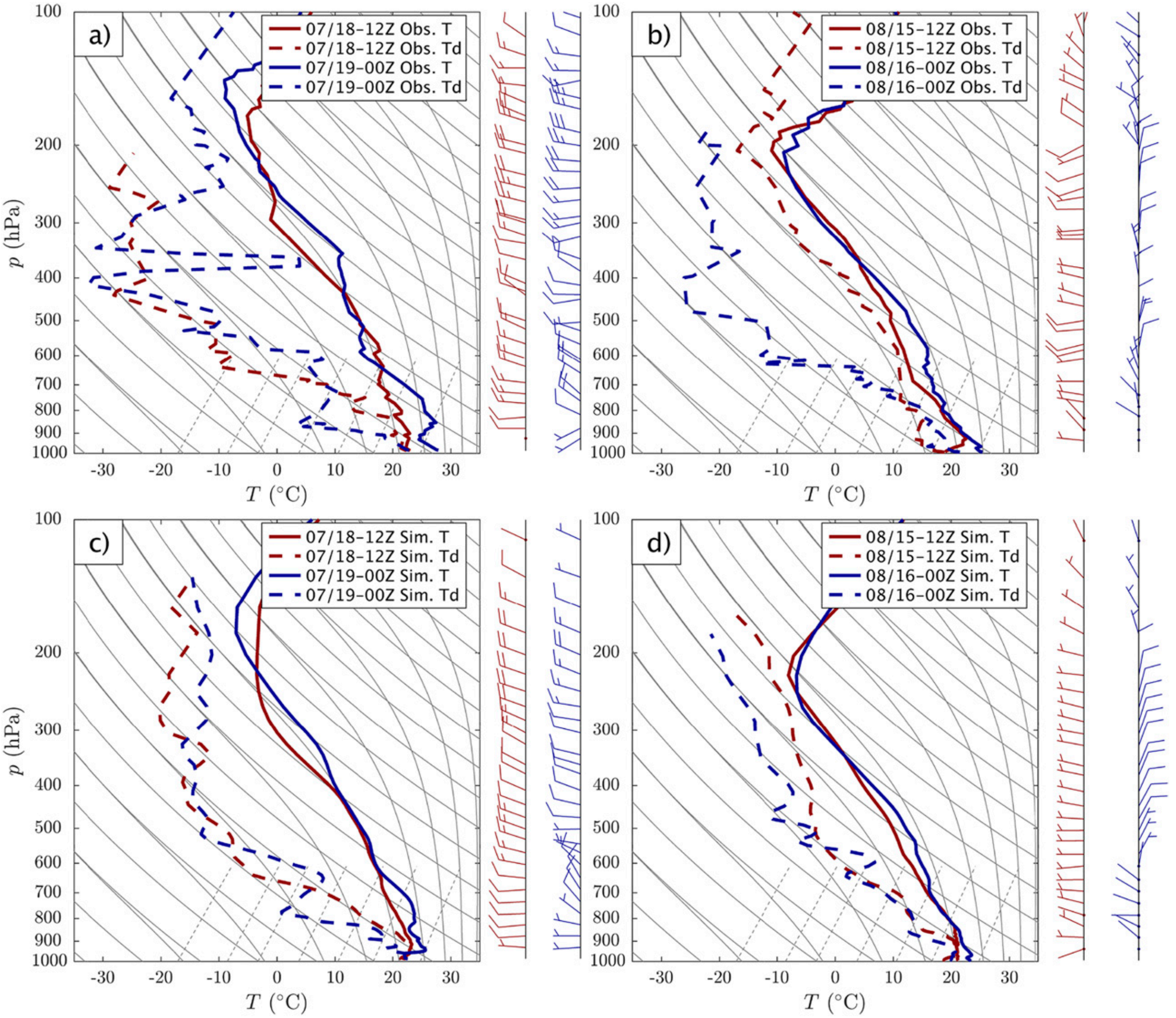

FIG. 7. Observed soundings at 1200 UTC (0800 EDT) and 0000 UTC (2000 EDT) at Buffalo for (a) 18 Jul and (b) 15 Aug 2015. Simulated soundings at 1200 UTC (0800 EDT) and 0000 UTC (2000 EDT) at Buffalo for (c) 18 Jul and (d) 15 Aug 2015.

of the Lake Ontario LBF in all directions (cf. Figs. 2 and 5). The mean surface θ_e in the ECPASS study region was slightly less than that in the July case (345 K). This difference in the surface θ_e was associated with lower near-surface relative humidity in this case (not shown).

Although, as shown above, the values of near-surface θ_e differ between the two cases, these values both sufficed to provide substantial moist instability. The mean-layer (0–500 m above ground) convective available potential energy (CAPE) from the Buffalo soundings reached 1096 J kg^{-1} at 0800 EDT and only decreased slightly to 1058 J kg^{-1} at 2000 EDT in the July case, while it increased from 69 to 1157 J kg^{-1} between 0800 and 2000 EDT in the August case, suggesting similar afternoon moist instabilities in the two cases. However, differences in large-scale forcing over the course of the day led to differences in convective inhibition (CIN). The CIN increased from 12 J kg^{-1} (0800 EDT) to 153 J kg^{-1} (2000 EDT) in the July case, compared to a decrease from 177 to 25 J kg^{-1} over the same period in the August case.

Although both cases exhibited mid- to upper-level warming during the day, the difference in diurnal CIN evolution may be attributed to the different layers over which this warming occurred. In the July case, the bulk of warming occurred across 850–650 hPa while the August case exhibited warming farther aloft (750–350 hPa). Thus, the low- to midlevel environmental lapse rate was more affected by the elevated warming in the former case. In their numerical experiments, McCaul and Weisman (2001) showed that, for all else equal, the low- to midlevel lapse rate controls convection intensity more strongly than does the upper-level lapse rate. Thus, despite the similar evening CAPE values in the two cases and similar degree of elevated warming, the lower height of the warming in the July case may have acted as a stronger brake on the lake-breeze-forced moist convection. Moreover, the prominent low- to midlevel drying in the July case likely further reduced parcel buoyancy through entrainment (e.g., Rousseau-Rizzi et al. 2017).

4. Numerical simulations

To provide a more quantitative analysis of the larger-scale and mesoscale forcing of deep convection in the two study cases, we conduct cloud-resolving, real-case numerical simulations using the Weather Research and Forecasting (WRF) Model, version 3.8.1 (Skamarock et al. 2008). WRF is a nonhydrostatic, compressible, time-split Eulerian numerical weather model that solves the 3D moist atmospheric equations on an Arakawa C staggered grid. The equations are integrated using the third-order Runge–Kutta scheme, with fifth-order horizontal and third-order vertical advection and positive definite scalar transport schemes. The simulations are initialized using the 6-hourly, 2000 EDT NAM analysis prior to each case study and are integrated for 24 h.

The simulations use three two-way nested domains (Fig. 8), the outermost of which covers large portions of the eastern United States and Canada with a horizontal grid spacing $\Delta x = \Delta y = 3$ km. The second domain covers the eastern Great Lakes and surroundings with $\Delta x = \Delta y = 1$ km. The innermost domain, which focuses on the ECPASS study area, has $\Delta x = \Delta y = 200$ m. This latter grid size is required to resolve narrow and turbulent LBFs, which are typically ~1 km wide (Chiba 1993; Wood et al. 1999; Samiro 2015), as well as boundary layer thermals and subcloud-scale drafts (Bryan et al. 2003). Unless otherwise stated, all model analysis is conducted on this finest domain. All domains use 101 hydrostatic pressure levels that are terrain-following at the surface and gradually relax to horizontal at the model top at 50 hPa. The nominal vertical grid resolution is ~20 m over the lowest 1 km, with the lowest level at ~10 m above ground. The top boundary is rigid and an implicit gravity wave damping layer is placed over the uppermost 5 km to prevent spurious wave reflections from the model top.

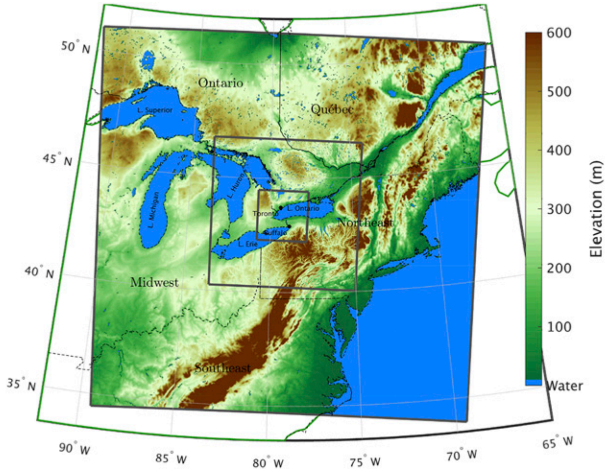

FIG. 8. The WRF simulation domain. The outermost domain (d01) uses $\Delta x = \Delta y = 3$ km, the intermediate domain (d02) has $\Delta x = \Delta y = 1$ km, and the innermost domain (d03) uses $\Delta x = \Delta y = 200$ m. The terrain elevation is indicated by the color shading.

The simulations parameterize longwave and shortwave radiation using the Rapid Radiative Transfer Model for global climate models (RRTMG) scheme. The Noah land surface scheme is used along with the Eta surface layer scheme employing Monin–Obukhov similarity theory and the Mellor–Yamada–Nakanishi–Niino (MYNN) third-order planetary boundary layer (PBL) scheme. Ocean and lake surface temperatures are prescribed using the surface skin temperature data in the 6-hourly NAM analysis, which is based on the daily Real-Time Global (RTG) analysis (Thiébaux et al. 2003) produced by the Marine Modeling and Analysis Branch of the National Centers for Environmental Prediction. Horizontal turbulent mixing is parameterized using a Smagorinsky-type closure. A single-layer urban canopy model is used in urban regions, and cloud microphysics are parameterized using the Thompson scheme with a fixed droplet number concentration of $N_c = 300\,\mathrm{cm}^{-3}$.

5. Simulation results

a. LBF tracking

To track the simulated LBFs, the simulated fields in the innermost domain are first interpolated onto new 3D grids with the same nominal vertical levels as in the WRF setup. The grid points are equally spaced in latitude and longitude distance, with the number of grid points in each horizontal dimension adjusted so that the Cartesian grid spacing is ~500 m (slightly coarser than the native model grid to save computational expense).

Three such interpolation grids are defined over the Niagara Peninsula, each with its long axis roughly paralleling the local lake shoreline. The first grid is placed over the southwestern section of Lake Ontario with its western and eastern limits extending roughly from Hamilton to mesonet station L6B (yellow box in Fig. 1). Another grid is specified farther east over central Lake Ontario (orange box in Fig. 1). The third grid covers the entire length of the Niagara Peninsula, parallel to Lake Erie's northern shore (red box in Fig. 1).

Since LBFs are usually associated with enhanced near-surface, shore-normal T, T_d, and/or wind gradients, we used the lowest-model-level fields (denoted ϕ, where ϕ represents a generic variable) to compute shore-normal derivatives (ϕ_n). For the wind gradient, the shore-normal wind component (here denoted $\tilde{u}$) is used. Then, for each alongshore transect on each interpolation grid, local extrema of ϕ_n are identified as potential LBF locations. For this analysis we applied nine-point smoothing to ϕ and ϕ_n to limit the influence of boundary layer thermals.

We first attempted to track the LBFs by checking the spatial coincidence in the gradients of different quantities. However, extensive examination suggested that the shore-normal wind gradient ($\tilde{u}_n$) alone best matched the LBF propagation apparent to the eye. Thus, we manually select the local $\tilde{u}_n$ minimum along each transect that, judging by the nearby wind directions, appears most representative of the LBF. This manual approach was ultimately deemed necessary given the difficulties in automatic tracking of LBFs in a highly turbulent flow.

Gaps along the analyzed LBFs sometimes arise in this analysis, in part due to the abovementioned smoothing. These missing values are filled using 1D piecewise Hermite polynomial interpolation. Due to its labor intensiveness, frontal tracking is only done in 30-min intervals during the daytime period of the simulations (0600–1800 EDT) for LBFs over the Niagara Peninsula (LBFs are also simulated to the north of Lake Ontario in both cases but are not tracked). We estimate the uncertainty in our frontal tracking analysis to be ±3 km, some of which results from the heavy smoothing. However, this smoothing is essential for minimizing false detections.

b. *Overview of the two cases*

The simulated LBFs for 18 July case evolve similarly to those observed (cf. Figs. 9 and 2): the Lake Erie LBF forms earlier and propagates inland faster than the Lake Ontario LBF to its north. As shown in the vertical cross section through the lake breezes at different times in Figs. 10a, 10c, and 10e, the onshore flow is generally about three times deeper behind the Lake Erie LBF than behind the Lake Ontario LBF. Between the two LBFs lies a west-southwesterly ambient flow of modest strength (2–4 m s^{-1}, increasing throughout the morning). The two LBFs begin to collide around 1300 EDT toward the eastern end of the peninsula, about 1–2 h before the same collision was observed. As the Lake Erie LBF continues its northward propagation, the merged zone extends westward. Showers initiate along the merged boundary, where local forcing for ascent is maximized (Figs. 9d and 10c). By 1630 EDT, the merged boundary has reached the southern shore of Lake Ontario (Figs. 9e and 10e). Isolated showers continue to initiate along this boundary but they are weaker than before. Consistent with the observations, scattered afternoon showers also develop north of Lake Ontario.

In the August case, a LBF is found along the southern shore of Lake Ontario at 1200 EDT in the observation but not in the simulation (cf. Figs. 11a and 5a). Although a weak onshore flow is simulated over the southern shore of Lake Ontario at this time, inspection of the simulated surface winds before this time suggests that this flow is not a lake breeze but the remnant of a weakening northerly background flow. The simulated southern Lake Ontario LBF forms at about 1300 EDT (not shown), implying a 1–2-h delay in the simulated LBF formation. After the simulated Lake Ontario and Lake Erie LBFs develop along their parent shores, they propagate inland nearly symmetrically as in the observation (cf. Figs. 11 and 5). As in the July case, the onshore flow behind the Lake Erie LBF is about twice as deep as that behind the Lake Ontario LBF (Fig. 10). The winds between these two LBFs are generally light and variable. The two LBFs begin to collide and initiate showers over the central peninsula by 1600 EDT (Figs. 10d and 11c). As the merged boundary progressively lengthens zonally and becomes quasi-stationary, so does the band of showers along it (Figs. 10f and 11c,d). A cluster of showers also develops just to the west of the Niagara Peninsula over 1600–1700 EDT, with higher coverage and intensity than that observed.

c. *Model verification*

1) SURFACE MESONET

To verify the simulated surface conditions and timing of LBF passage, we interpolate the model output to mesonet stations W5Z and A0T, located along the mesonet transect over the Niagara Peninsula (Fig. 1). Although other mesonet stations also exist along the transect (e.g., L6A and L6B), the chosen inland stations are better positioned to observe transient LBF passage than the stations located along the shorelines, which persistently observe onshore flow (not shown). Because only the observed and simulated Lake Erie LBF reach both stations in each case, we focus on the propagation of this LBF in this analysis.

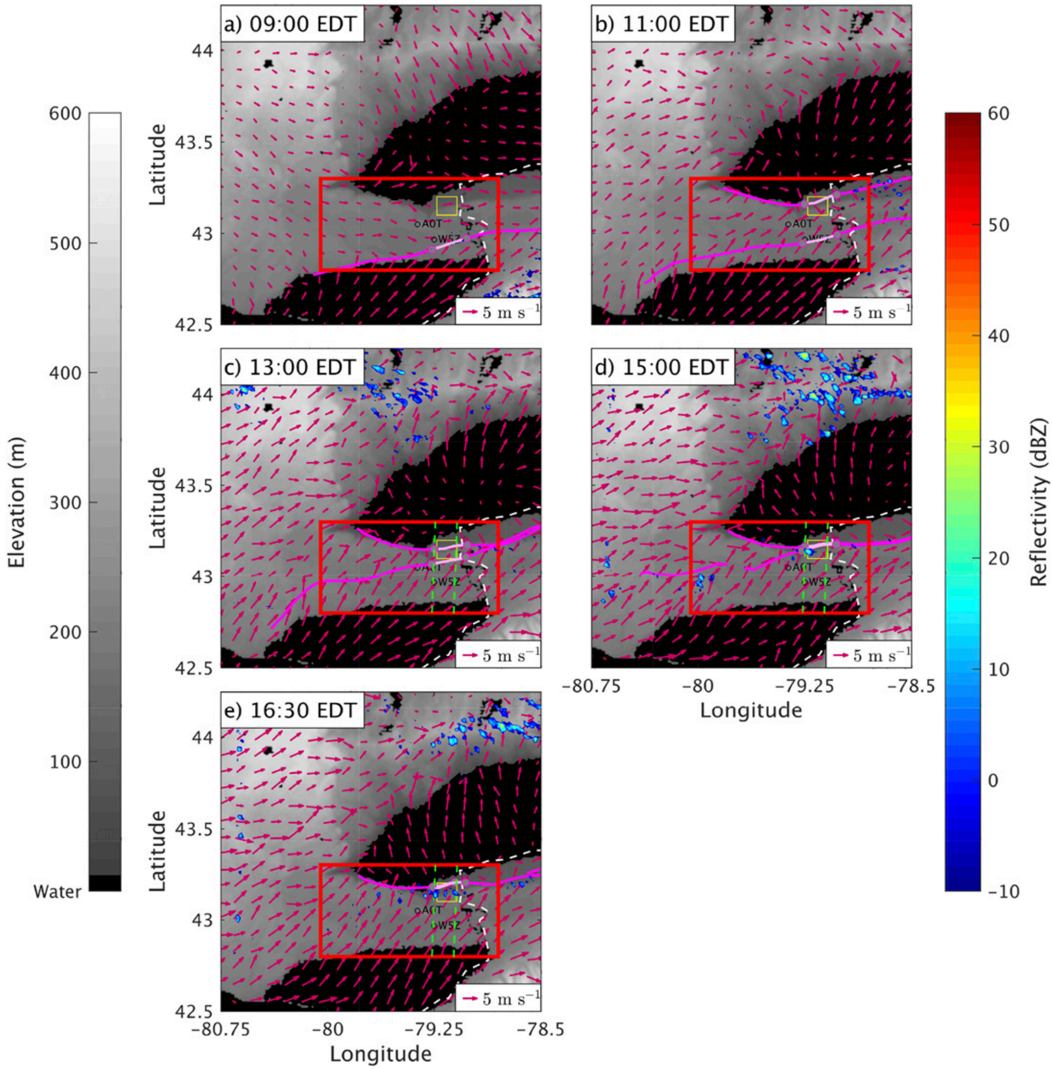

FIG. 9. Simulated lowest-model-level radar reflectivity (color shading), 10-m winds (purple arrows), and analyzed positions of LBFs (purple lines) based on the model data at (a) 0900, (b) 1100, (c) 1300, (d) 1500, and (e) 1630 EDT 18 Jul 2015. The terrain profile is plotted in gray shading. The highlighted segments of the simulated LBFs indicate where various lake-breeze and LBF properties are computed. The yellow box indicates the areas where the areal averaging of simulated soundings in section 6a are performed. The green dashed lines show the western and eastern boundaries of the region where zonal average was computed for the cross sections in Fig. 10.

In the July case, both the observed and simulated T at these stations begin to rise steadily after sunrise (Fig. 12a). The simulated T at both stations are about 2°–3°C warmer than that observed before noon but better match the observations after noon. Both the observed and simulated T at station W5Z show a reduced warming rate or even a slight cooling after the passage of the northern Lake Erie LBF. At station A0T, a reduced warming rate is already seen in the observation a few hours before the LBF passage. During this time, the observed solar radiation flux (F_s) decreased from ~800 to 500 W m^{-2}, indicating the presence of prefrontal clouds. The simulation does not capture this latter effect, as the warming rate and F_s do not show evidence of cloud cover prior to frontal passage. The simulated Lake Erie LBF crosses these stations 0.5–1.5 hours earlier than observed, suggesting modest errors in the simulated state of the atmosphere and LBF propagation.

In contrast, the simulated T at stations A0T and W5Z on 15 August are both about 2°–3°C cooler than those observed, with the errors again gradually decreasing over time (Fig. 12b). At station W5Z, the simulated Lake Erie LBF passage leads to a cessation of diurnal warming, which is not unexpected but disagrees with

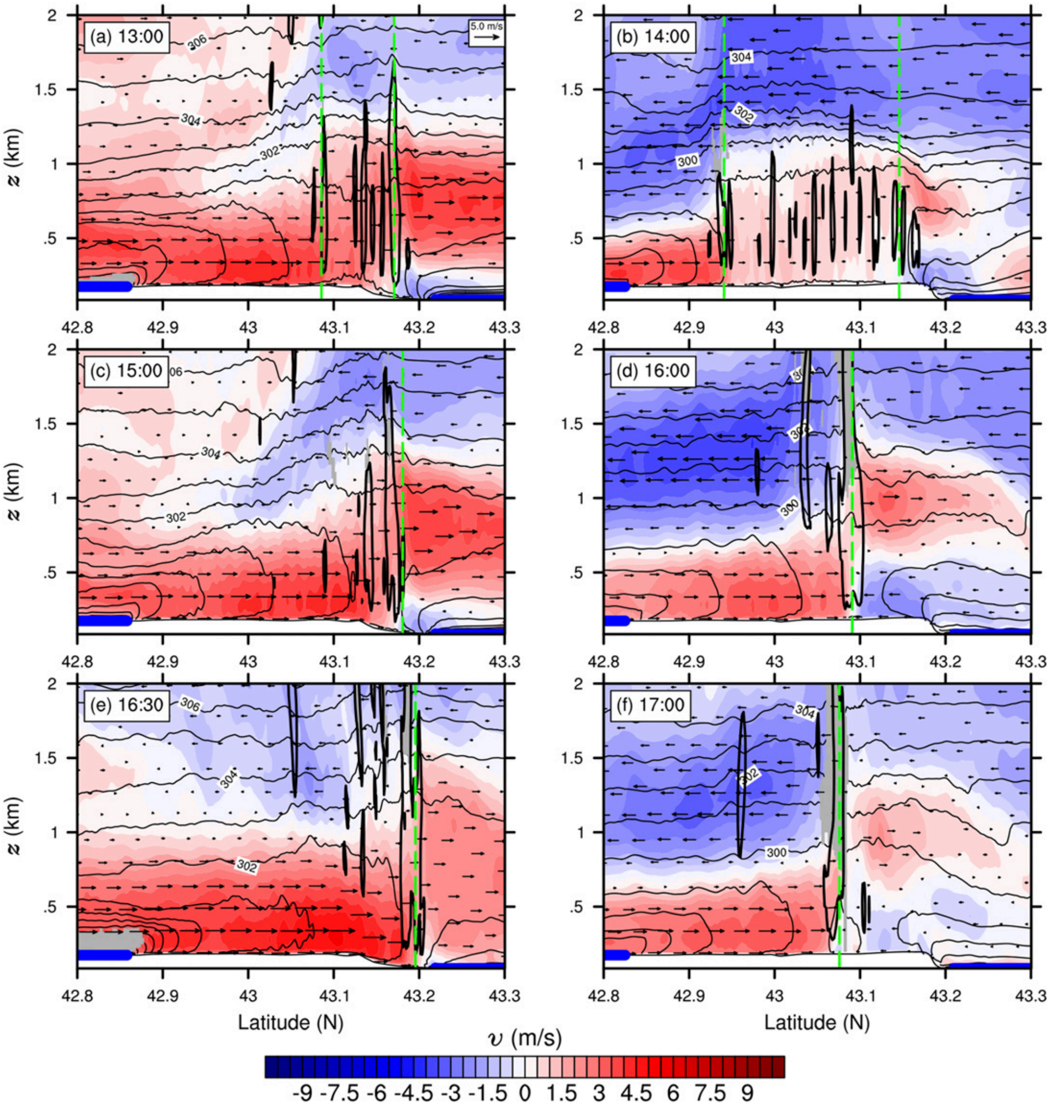

FIG. 10. Zonally averaged cross sections of simulated meridional wind (red/blue shading), plane-parallel wind vectors (arrows), potential temperature in 1-K intervals (thin black lines), vertical motion = 0.2 m s^{-1} (thick black contour), approximate locations of simulated LBFs (green dashed lines), and liquid water mixing ratio = 0.075 g kg^{-1} (gray shading) at (left) 1300, 1500, and 1630 EDT 18 Jul 2015 and at (right) 1400, 1600, and 1700 EDT 15 Aug 2015. The regions where the cross sections are computed are shown in Figs. 9 and 11.

the observation (where surface warming continued after LBF passage). Similar to the July case, both the observation and simulation exhibit a reduced warming rate at station A0T 1–2 h prior to the frontal passage. During this period, both the observed and simulated F_s decrease from ~800 to ~300 W m^{-2}, again suggesting the presence of prefrontal clouds. Compared to the 18 July case, there is less timing error in the simulated LBF crossings (20 min vs 0.5–1.5 h), thus indicating a more accurate model representation of the LBF in this event.

The impact of LBF passage on low-level moisture is less evident, possibly because of a complex sensitivity of low-level humidity to lake-breeze passage. Although the onshore flow behind the LBF tends to have higher relative humidity than prefrontal air, the latter may still possess larger specific humidity due to its higher T. On 18 July, the observed water vapor mixing ratio (q_v) at stations A0T and W5Z increased during the morning but decreased slightly after Lake Erie LBF passage (Fig. 12c). The larger q_v in the nominally warmer and drier prefrontal air may stem from strong evapotranspiration, and hence large latent heat fluxes, over land. Over Lake Erie, cooler temperatures and higher humidity of lake-cooled air generally limit the latent

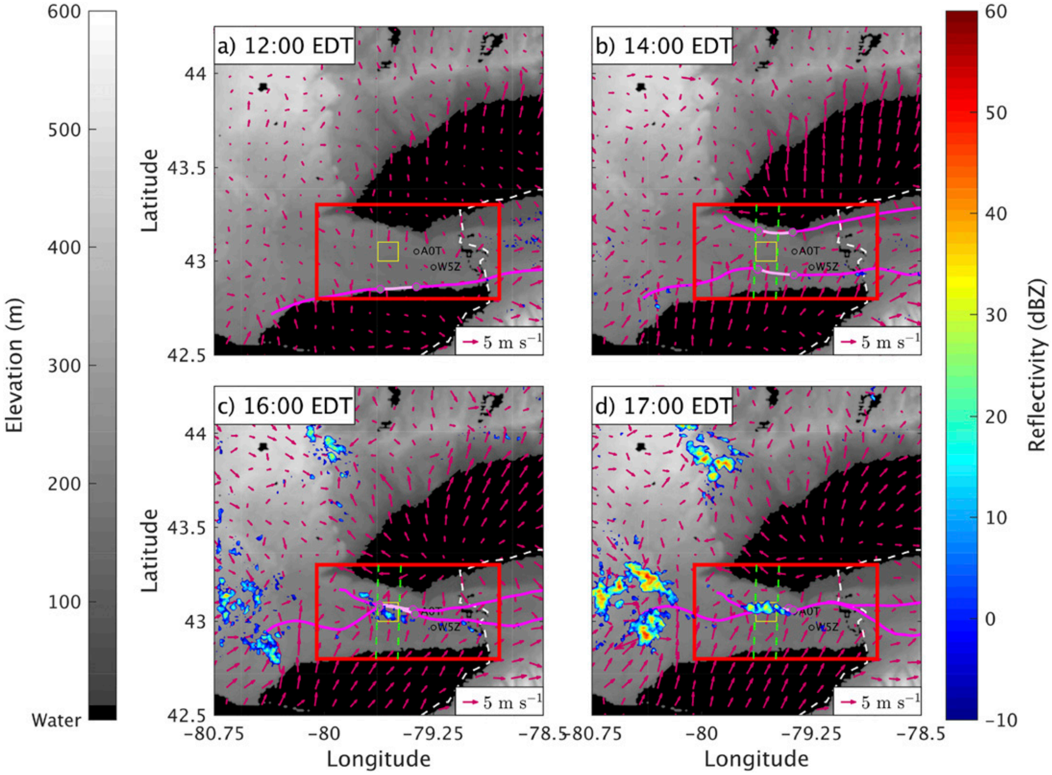

FIG. 11. As in Fig. 9, but for (a) 1200, (b) 1400, (c) 1600, and (d) 1700 EDT 15 Aug 2015.

heat fluxes, leading to smaller q_v behind the LBF. This subtlety is not captured in the simulation, where q_v is nearly constant throughout the day at station W5Z and fluctuates at station A0T without showing a clear signature of LBF passage. On 15 August, the observed q_v increased at both stations after the LBF passage (Fig. 12d). The simulation reproduces this pattern despite a slight overall underprediction in q_v.

The observed wind speed (V) on 18 July was already increasing at stations W5Z and A0T before the Lake Erie LBF passage, as the background flow strengthened in the morning (Fig. 12e). It continued to increase after the LBF passage as the lake-breeze flow superimposed on the strengthening background flow. The wind direction ($\angle V$), on the other hand, did not show a clear change after the frontal passage (Fig. 12g). Although northwesterly winds briefly prevailed between 0800 and 1000 EDT, the background flow shifted to southwesterly well before LBF passage and remained so thereafter. Overall, the simulation adequately captures the observed diurnal evolution of the surface winds despite a 1–2 m s^{-1} overprediction in V before noon, which may have contributed to the overly fast simulated LBF propagation.

On 15 August, a light southwesterly wind also prevailed at station W5Z before the LBF passage and only a slight (~0.5 m s^{-1}) increase in V was observed after the frontal passage (Fig. 12f). The simulation captures the bulk of the observed wind pattern except for an underestimation of 0.5–1.5 m s^{-1} in wind speed and a more variable $\angle V$ before LBF passage (Figs. 12f,h), the former possibly leading to the slight delay in the LBF passage over this station. The observed winds at station A0T were generally light throughout the day until LBF passage at around 1600 EDT, when they shifted to southwesterly. The simulation captures the weak winds throughout the day as well as the rapid wind shifts associated with LBF passages.

To extend the model verification to the entire domain, observations from all mesonet stations are used to compute the model daytime (0600–1800 EDT) averaged root-mean-squared error (RMSE) and bias (or mean error; e.g., Wilks 2011; AL-Lami et al. 2017) of T, q_v V, and $\angle V$ (Table 1). In both cases, the RMSE and bias for T and q_v are ~2°C and 1.5 g kg^{-1} or less, suggesting a reasonable match between model and observations. More prominent errors are found in the RMSE of wind velocity, in that the speed errors are comparable to V itself and the directional errors are between 45° and 90°. We speculate that the latter arises from the turbulent nature of the convective boundary layer, which gives rise to chaotic and high-frequency

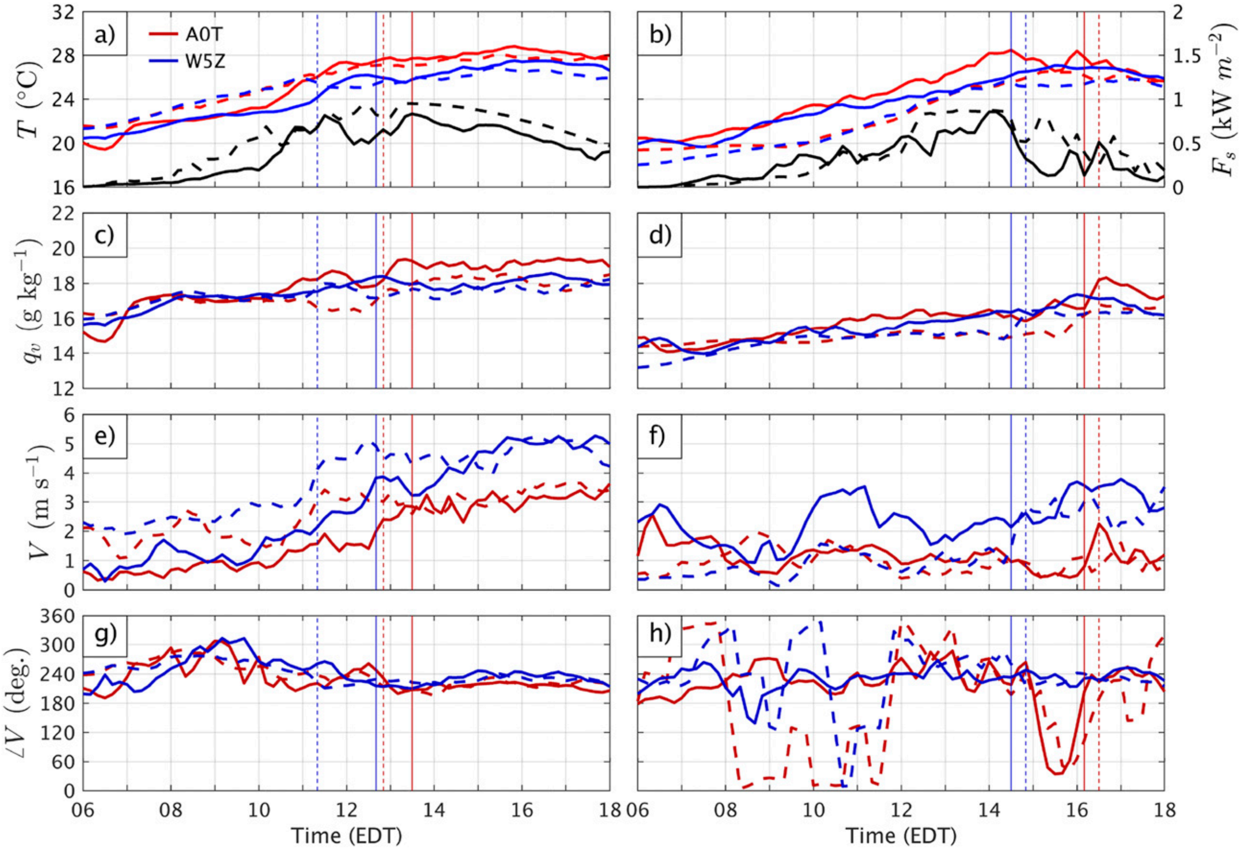

FIG. 12. Time series of observed (solid) and simulated (dashed) air temperature (T), water vapor mixing ratio (q_v), wind speed (V), and wind direction ($\angle V$) at mesonet stations A0T and W5Z on (left) 18 Jul 2015 and (right) 15 Aug 2015. The black lines in (a),(b) represent the observed (solid) and simulated (dashed) solar radiation flux at mesonet station A0T on 18 Jul and 15 Aug, respectively. The vertical lines indicate the times of the observed (solid) and simulated (dashed) Lake Erie LBF arrival at each station.

wind fluctuations. The relatively small bias of both cases suggests that the multi-station-averaged simulated winds are far more accurate than the instantaneous winds at a single location.

2) RADIOSONDES

We evaluate the model soundings through comparison against the Buffalo operational soundings (Fig. 1). Although special soundings were available from King City (on 18 July only), these were plagued by high-amplitude noise and not used. In the July case, the evolution of T and T_d above 600 hPa is accurately simulated (Fig. 7c). Although midlevel warming is simulated during the daytime, its magnitude is underestimated by 1°–3°C and the resulting warm layer is ~100 hPa too shallow. These errors lead to a weaker simulated midlevel (850–600 hPa) capping inversion during the late afternoon, and thus a smaller low-level static stability than that observed.

Although the simulation underestimates the low- to midlevel static stability, it also shows a ~3°C underprediction in the near-surface T at 2000 EDT (cf. Figs. 7a,c), stemming from an earlier onset of surface radiative cooling. As a result of these offsetting errors, the simulated 500-m AGL mean-layer CIN is similar to that observed in the 2000 EDT Buffalo sounding (169 vs 153 J kg^{-1}). However, the simulated daytime CAPE evolution differs notably from the observation, with the former decreasing from 1468 J kg^{-1} at 0800 EDT to 378 J kg^{-1} at 2000 EDT and the latter staying relatively constant near 1000 J kg^{-1} throughout the day.

TABLE 1. Daytime averaged simulation RMSE and bias of air temperature (T), water vapor mixing ratio (q_v), wind speed (V), and wind direction ($\angle V$) at the mesonet stations for both events.

	T (°C)	q_v (g kg^{-1})	V (m s^{-1})	$\angle V$ (°)
		18 Jul		
RMSE	1.6	1.3	1.4	63.5
Bias	−0.6	0.3	0.5	10.3
		15 Aug		
RMSE	2.3	1.6	1.3	85.0
Bias	−1.7	1.0	0.3	12.9

The model also captures the observed low- to midlevel drying, but overestimates the base height of this drying by ~100 hPa and underpredicts T_d by 3°–6°C. Finally, although the simulation broadly captures the wind direction, it underestimates the wind speed above 300 hPa by about 3 m s^{-1} at both times.

The model also captures the general diurnal evolution of T at Buffalo in the August case, except for a 1°–3°C underestimation in the daytime midlevel warming (Fig. 7d). The simulated T_d is much too low in the mid- to upper levels at 0800 EDT but generally improves at 2000 EDT. The simulated CAPE at 0800 EDT is much larger than that observed (1189 vs 69 J kg^{-1}) because of the warmer and moister simulated boundary layer (cf. Figs. 7b,d). Consequently, the simulated CIN at that time is also much smaller than the observed (37 vs 177 J kg^{-1}). By 2000 EDT, the simulated CAPE and CIN values reached 1390 and 25 J kg^{-1}, respectively, which compare well with the observations (CAPE = 1157 J kg^{-1} and CIN = 25 J kg^{-1}). The simulation also captures the wind shift aloft (above 600 hPa) from generally westerly early in the day to mostly northerly later in the day.

The tropospheric relative humidity differs in the two events, with the 15 August case exhibiting smaller dewpoint depressions (and hence larger relative humidities) over the 900–700-hPa layer. In drier flows, entrainment of environmental air into the cumuli leads to increased evaporative cooling, which tends to weaken the cumuli and limit their growth (e.g., Derbyshire et al. 2004; Rousseau-Rizzi et al. 2017). Thus, the drier atmosphere in the 18 July case may lead to stronger entrainment-induced suppression of ascending cumuli than in the August case.

3) CONVECTION INTENSITY

We evaluate the simulated convection intensity through comparison to the observed maximum radar reflectivity and echo-top height over the Niagara Peninsula from the King City radar. For consistency with the former calculation, we linearly interpolate the simulated reflectivity to the height of King City radar's lowest elevation angle. No such interpolation is performed for the echo-top height. The filtering criteria applied to the observations in section 3 are also applied to the simulations, except for the differential reflectivity and copolar correlation coefficient thresholds (since all simulated reflectivity is free of artifacts).

In the 18 July simulation, the maximum echo top over the Niagara Peninsula is around 3 km MSL, 2–3 km shallower than that observed (Figs. 4b,d). However, the observed echo tops only exceeded 4 km for a short time (~30 min) immediately after the LBF collision. In the simulation, scattered showers with lower echo tops persist over the peninsula for several hours after LBF collision at ~1400 EDT (Figs. 4c,d). The maximum simulated reflectivity agrees well with the observation (35 dBZ), reaching ~30 dBZ by midafternoon before weakening to ~20 dBZ later (Figs. 4a,c).

Although the simulation of 15 August does not capture the observed early morning showers associated with a departing disturbance, both the simulated maximum reflectivity and echo-top height associated with LBF-forced convection agree well with the observations (Fig. 4). The simulated maximum radar reflectivity reaches ~45 dBZ during the late afternoon as compared to 50 dBZ in the observation. The maximum simulated echo-top height reaches ~7 km MSL, close to the observed value of ~8 km. The timing of simulated LBF-forced moist convection overall agrees well with the observation, in that showers appear about an hour before Lake Ontario and Lake Erie LBF collision and intensify shortly thereafter.

Arguably the most prominent errors in the simulations are the too-low echo tops and persistent light precipitation on 18 July, as well as the failure to capture the early morning showers on 15 August. Such errors could stem from a multitude of factors, including (i) biases and/or lack of mesoscale detail in the initial conditions, (ii) cloud-microphysics schemes generate precipitation too readily in shallow convection (Wang and Kirshbaum 2015), and (iii) errors in parameterized surface fluxes and/or boundary layer transport. Nevertheless, the many areas of agreement between the observations and simulations, particularly in reproducing the differences in convection intensity between the two cases, suggest that the simulations can offer useful insights into the factors responsible for these differences.

6. Forcing of moist convection

a. Large-scale forcing

One of the key differences between the 18 July and 15 August cases is that the former exhibited much stronger midlevel warming during the daytime (Fig. 7), which helped to suppress convection in the afternoon. To examine this warming in detail, we analyze simulated synoptic-scale vertical motion and temperature advection. For this analysis, we first smooth the simulated wind and temperature fields from the outermost simulation domain (d01, Δx = 3 km) onto a coarser grid with 100-km resolution. These smoothed fields are then interpolated vertically onto pressure levels. To diagnose the large-scale forcing of vertical motion, we evaluate the quasigeostrophic (QG) ω equation over

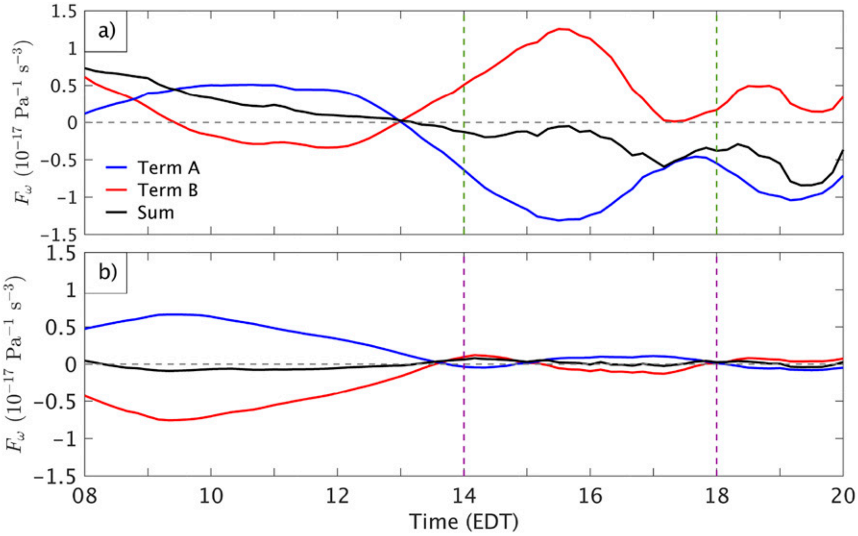

FIG. 13. Time series of simulated QG-ω forcing terms averaged over the Niagara Peninsula for (a) 18 Jul and (b) 15 Aug 2015. The vertical dashed lines indicate the time period of active lake-breeze-forced convection in the simulations.

the 850–650-hPa layer (where the strongest warming occurred in the July case):

$$\left(\sigma\nabla_p^2 + f_0^2\frac{\partial^2}{\partial p^2}\right)\omega = \underbrace{-f_0\frac{\partial}{\partial p}[-\mathbf{V}_g\cdot\nabla(\zeta_g+f)]}_{\text{A}} \underbrace{-\frac{R}{p}\nabla_p^2(-\mathbf{V}_g\cdot\nabla T)}_{\text{B}}, \tag{1}$$

where f_0 is the Coriolis parameter at a reference latitude of 43°N, R is the gas constant of dry air, $\mathbf{V}_g$ is geostrophic wind vector, ζ_g is the geostrophic relative vorticity, σ is the atmospheric static stability parameter $(RT/p)(\partial\ln\theta/\partial p)$, where θ is the potential temperature. Term A on the right-hand side of (1) is proportional to the vertical differential of absolute vorticity advection and term B is proportional to the horizontal Laplacian of temperature advection. The effects of diabatic heating and friction are neglected. The left-hand side of (1) is like a Laplacian operator, so, given $\omega = 0$ boundary conditions, it is roughly proportional to $-\omega$ (and hence vertical motion). Thus, a positive right-hand side tends to force ascent and vice versa.

On 18 July, the sum of terms A and B averaged over the Niagara Peninsula is positive at 0800 EDT but gradually decreases to negative values by 1300 EDT (Fig. 13a). Based on the simulated 850–650-hPa flow during this period, the study region is positioned between a midlevel trough and a ridge with positive differential vorticity advection and locally weak warm advection (relative to the surroundings) (Figs. 14a,b,d,e). As a result, term A is strongly positive and term B is negative between 0930 and 1300 EDT, with a positive net forcing for ascent (Fig. 13a). By midafternoon, the ridge builds into southern Ontario (Figs. 14g–l) and both forcing terms switch sign (Fig. 13a), leading to a net forcing for descent.

On 15 August, term A is again positive and term B is negative before 1400 EDT (Fig. 13b). However, unlike the July case, these terms approximately cancel and lead to a nearly zero QG-ω forcing over the 850–650-hPa layer. This cancellation, and its minimal resulting forcing for ascent, continues after 1400 EDT, as terms A and B both weaken. Although this case experienced negative vorticity advection and thus net forcing for descent higher aloft (Fig. 6b), this forcing has minimal impact on the 850–650-hPa layer of interest.

Thus, along with horizontal warm advection, subsidence warming associated with large-scale descent also occurred on the afternoon of 18 July in the midlevels. To isolate the effect of each process, we compute the simulated profiles of potential temperature change due to horizontal and vertical advection from 1200 to 0000 UTC (0800–2000 EDT) interpolated onto a point in the middle of the Niagara Peninsula (43.0°N, 79.4°W). On 18 July, horizontal advection leads to ~2°C warming across the 850–650-hPa layer while subsidence-induced vertical advection causes 1°–2°C warming over the same layer (Fig. 15a). On 15 August, by contrast, horizontal advection minimally affects θ across the 850–650-hPa layer and

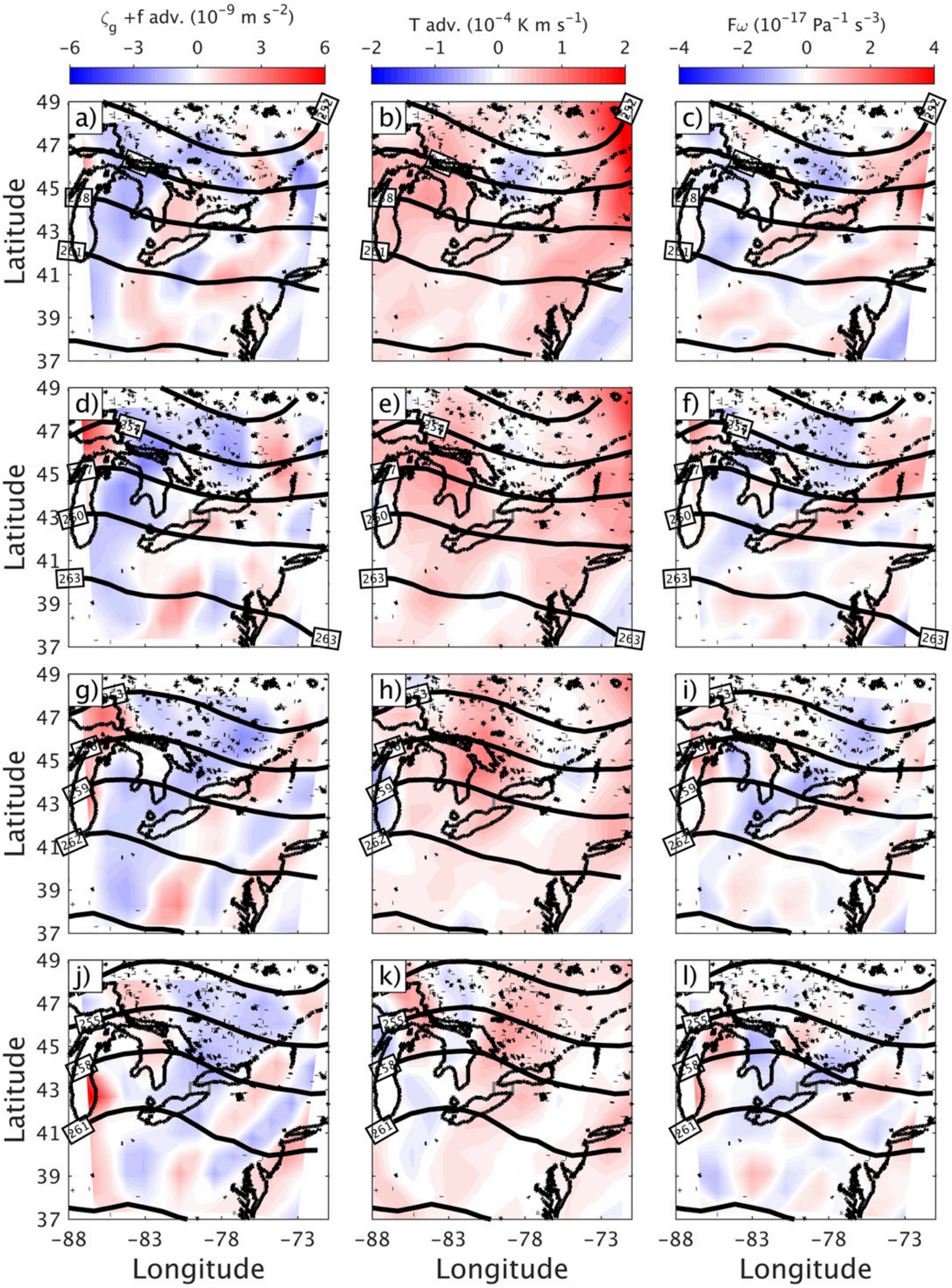

FIG. 14. (left) Simulated absolute vorticity advection (red/blue shading) and averaged geopotential height (solid contours) in the 850–650-hPa layer, (middle) horizontal temperature advection (red/blue shading) and averaged geopotential height (solid contours) in the same layer, and (right) QG-ω forcing (the sum of the right-hand side of (1); red/blue shading) and averaged geopotential height (solid contours) in the same layer. Four times are shown: (a)–(c) 0800, (d)–(f) 1100, (g)–(i) 1400, and (j)–(l) 1700 EDT 18 Jul 2015.

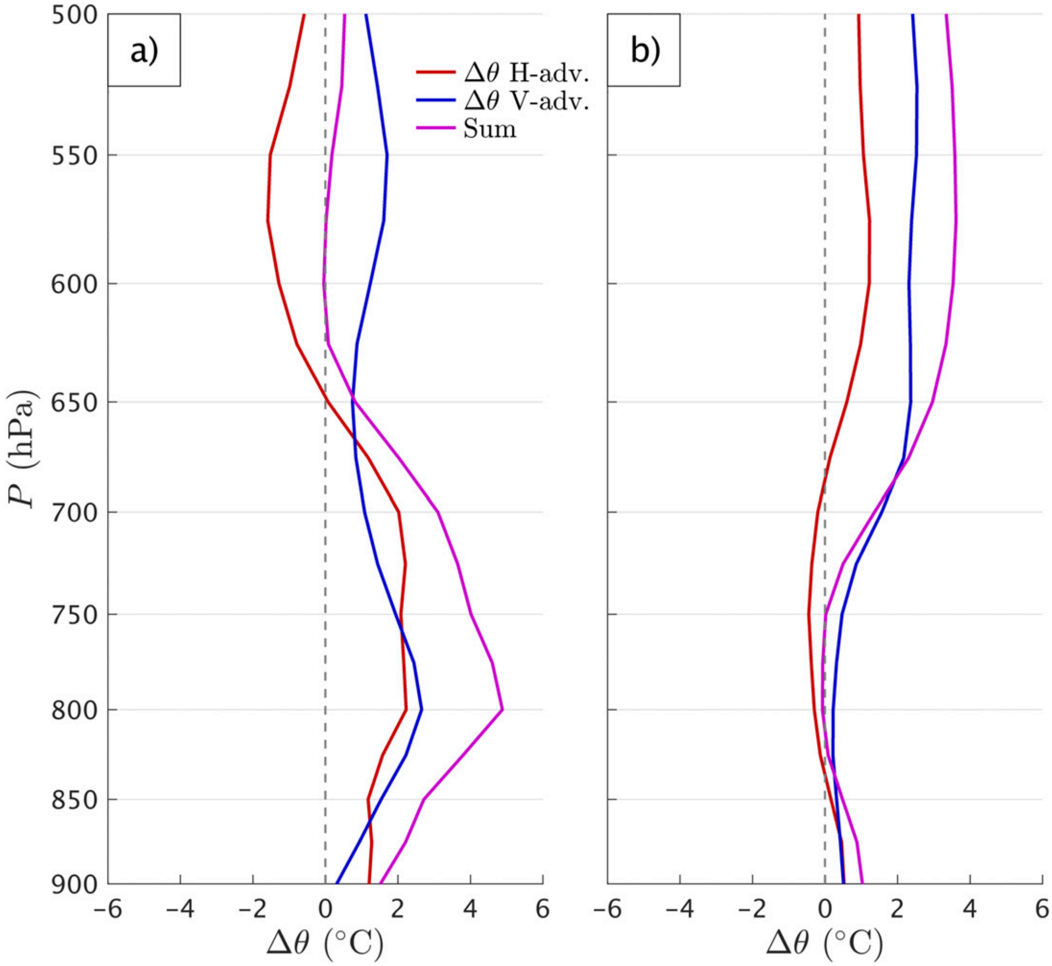

FIG. 15. Profiles of simulated potential temperature change between 1200 and 0000 UTC (0800–2000 EDT) due to horizontal and vertical advection at a point (43.0°N, 79.4°W) in the middle of the Niagara Peninsula for (a) 18 Jul and (b) 15 Aug 2015.

vertical advection only warms the atmosphere above 750 hPa (Fig. 15b).

To better visualize the impacts of the midlevel warming on the convective environment, we compute the averaged simulated sounding and parcel ascent profile over areas where simulated moist convection initiates (see Figs. 9 and 11 for the averaging locations). In the July case, adiabatically lifted parcels at the time of first simulated convection initiation (1400 EDT) can only generate marginal positive buoyancy over the 900–700-hPa layer due to the midlevel warming (Fig. 16a). This warming intensifies over time as a result of both the strengthening horizontal advection and subsidence warming, the latter of which also produces drying. A temperature inversion eventually develops, which effectively caps convection at 750 hPa (or 2–3 km MSL. Figures 16b and 16c). In the August case, because the warming occurs higher aloft (750–350 hPa), parcels can gain more buoyancy and ascend higher prior to encountering the warmed layer (Figs. 16d–f).

b. *Mesoscale forcing*

Another factor regulating convection intensity is the boundary layer forcing for ascent (e.g., Rousseau-Rizzi et al. 2017). To quantify and compare such forcing between the two cases, we compute various simulated properties averaged along specific segments of each LBF where moist convection is simulated, mainly during or after the LBF collision (note that the locations discussed herein differ from those above). These include the mean 10-m shore-normal wind speed from the LBFs to the parent lake shores (u_n), LBF propagation speed (C), and maximum cross-frontal mean vertical motion within the lowest 1 km above ground (w_{LBF}) and ±1.5 km of the LBF. The first two quantities are computed on the same shore-parallel grids previously

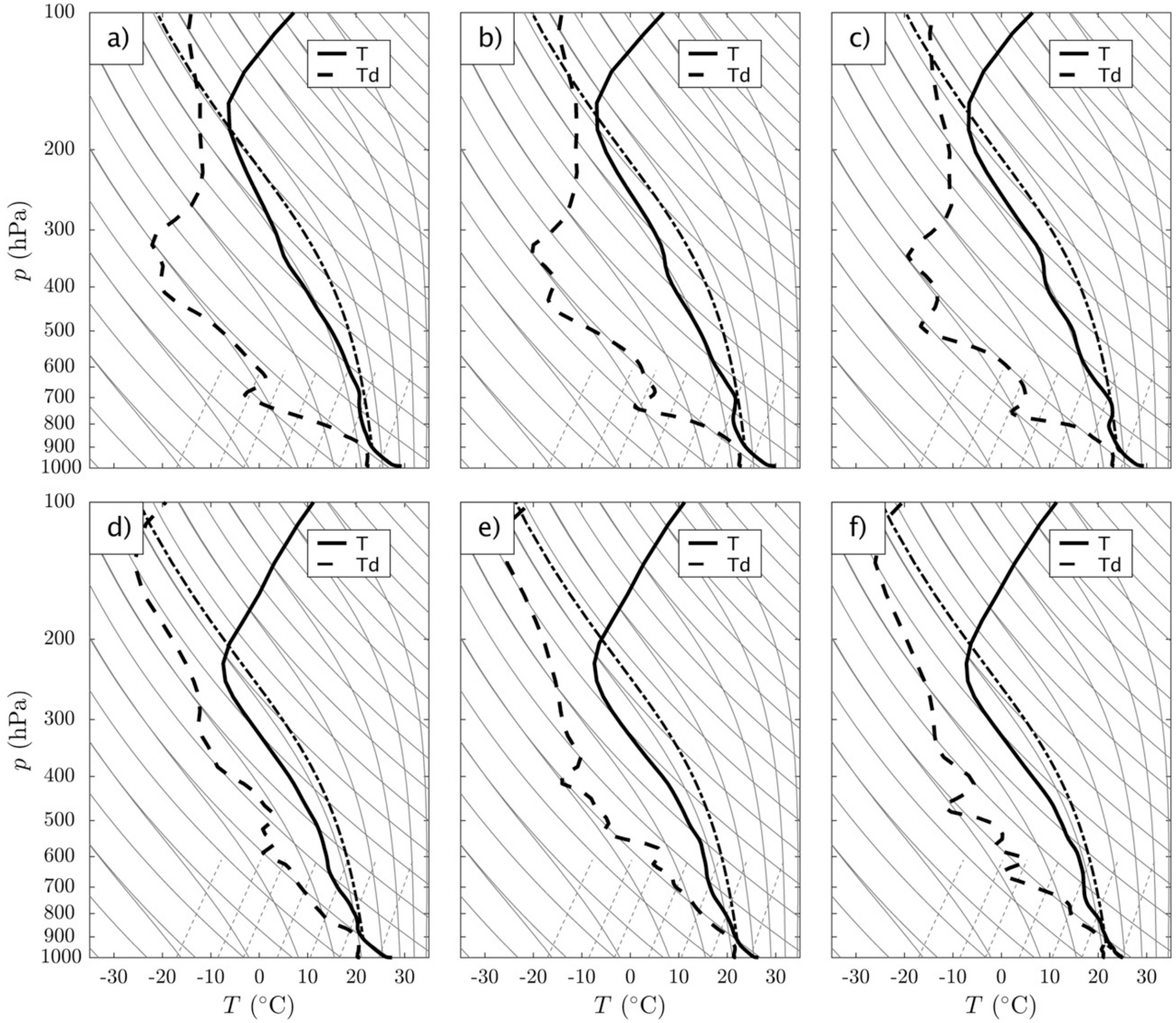

FIG. 16. The averaged simulated environmental sounding and parcel ascent profile over the areas where precipitating convection is simulated along the lake-breeze convergence zone (see Figs. 9 and 11 for the averaging areas) at (a) 1400, (b) 1600, and (c) 1800 EDT 18 Jul 2015, and at (d) 1500, (e) 1700, and (f) 1900 EDT 15 Aug 2015.

described in section 5a. The third further incorporates a vertical grid of terrain-following levels with 100-m grid spacing from the surface up to 1 km above ground. This latter height is based on past findings that the low-level convergence associated with LBFs is typically less than 1 km deep (Moroz 1967; Lyons 1972; Keen and Lyons 1978). Therefore, the strongest LBF-induced updraft should also reside within the lowest 1 km. Although not shown, the maximum cross-frontal averaged updraft velocities along all LBF segments are indeed found within 400–600 m above ground.

As an aid to interpretation, we also evaluate various simulated environmental quantities that are expected to regulate LBFs, based on the sea-breeze literature (e.g., Arritt 1993; McKendry and Roulet 1994; Atkins and Wakimoto 1997; Steyn 2003). One such quantity is the land–lake temperature difference ΔT ($\Delta T = T_l - T_w$), where T_l is the mean T over the land between the LBF segment of interest and 5 km ahead of it and T_w is the mean T over the parent water body (both are averaged vertically over 0–500 m above ground). Another is the ambient shore-normal wind (U_n), which is represented by the 10-m shore-normal wind averaged over the 5 km just ahead of the LBF segments. Although low-level stability is often considered to be another controlling parameter, the convective boundary layer is similarly stratified in both cases (not shown).

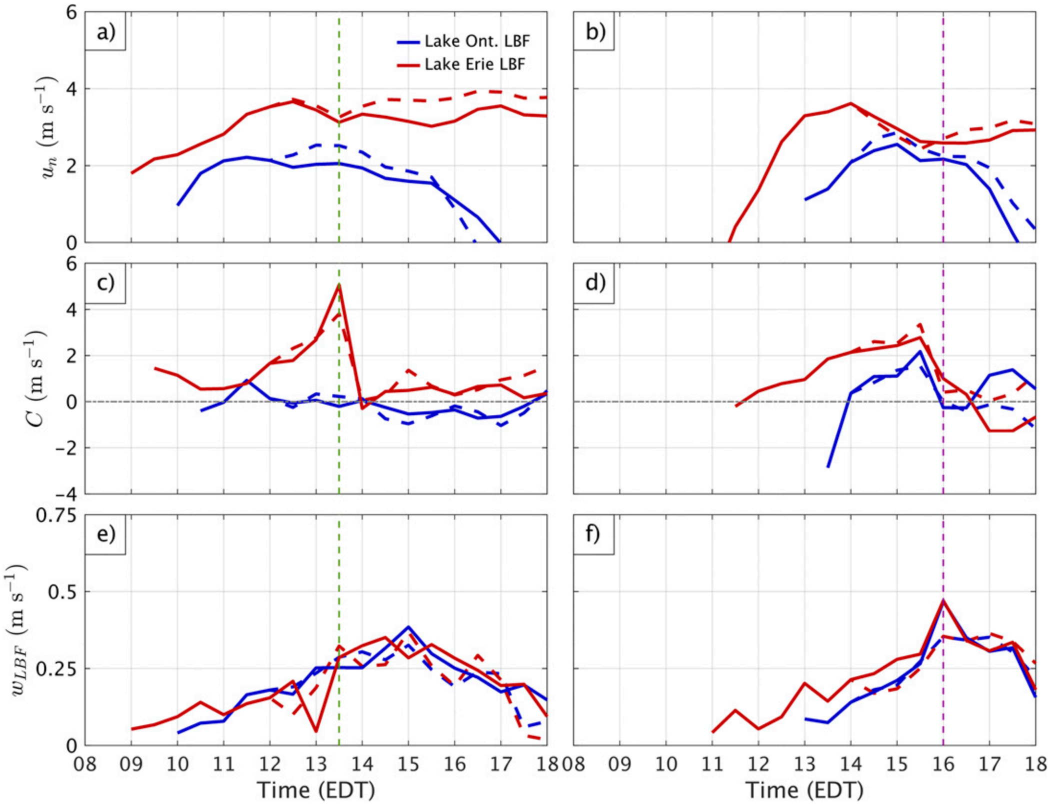

FIG. 17. Time series of simulated average lake-breeze onshore flow speed (u_n), average LBF propagation speed (C), and maximum cross-frontal averaged vertical velocity within the lowest 1 km above ground (w_{LBF}) for the lake breezes of (left) 18 Jul 2015 and (right) 15 Aug 2015. The vertical dash lines indicate the times of simulated LBF collisions. The solid lines correspond to the original simulations for each case, and dashed lines correspond to simulations where latent heat release is eliminated around 2 h prior to the time of frontal collision. The LBF segments over which these quantities are averaged are shown in Figs. 9 and 11.

1) 18 JULY

The simulated onshore flow behind the Lake Erie LBF (u_n) increases from ~2 m s^{-1} at the time of formation to ~4 m s^{-1} at around noon and remains nearly steady for the rest of the day (Fig. 17a). The early acceleration of this onshore flow likely stems from a combination of a 1–2 m s^{-1} increase in background wind (U_n) and an increasing ΔT during the morning (Figs. 18a,c). After 1200 EDT, u_n behind the Lake Erie LBF becomes quasi steady as the background winds and ΔT level off. For the Lake Ontario lake breeze, u_n also increases from 1 to 2 m s^{-1} at around noon (Fig. 17a) but later weakens as its ΔT diminishes and the opposing ambient winds increase (Figs. 18a,c). Comparing the two lake breezes, the Lake Ontario breeze onshore flow is ~1.5 m s^{-1} weaker than that of Lake Erie breeze due to its smaller ΔT and offshore ambient winds.

Similarly, the onshore propagation speed C of the simulated Lake Erie LBF is 1–3 m s^{-1} larger than that of the Lake Ontario LBF until LBF collision at ~1400 EDT (Fig. 17c). After the collision, the merged boundary slowly propagates northward toward Lake Ontario, which corresponds to a small onshore motion (positive) for the Lake Erie LBF, and vice versa for the Lake Ontario LBF. The small differences in C between the two LBFs after collision results from the different orientations of the tracking grids and the aforementioned uncertainties in the frontal position.

As the LBFs form and strengthen in the morning, w_{LBF} gradually increases to a maximum shortly after the LBF collision (Fig. 17e). The Lake Ontario LBF updraft slightly exceeds that of the Lake Erie LBF between 1100 and 1300 EDT, consistent with previous findings that sea-breeze frontogenesis is enhanced under offshore background winds (Arritt 1993; Atkins and Wakimoto 1997). After the LBFs collide, w_{LBF} along the merged boundary hovers around 0.3 m s^{-1} before diminishing after 1700 EDT as the merged boundary reaches Lake Ontario (Fig. 9e).

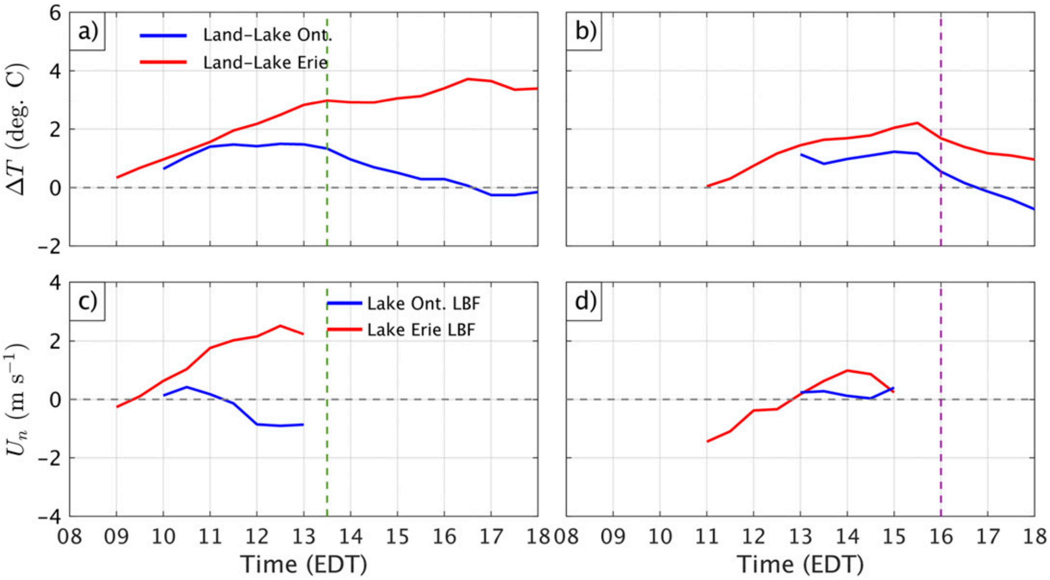

FIG. 18. Time series of simulated land–lake air temperature contrast (ΔT) and shore-normal wind speed ahead of the LBFs (U_n) for the lake breezes of (left) 18 Jul 2015 and (right) 15 Aug 2015. The vertical dash–dotted lines indicate the times of simulated LBF collisions. To focus on the ambient flow, the time series of U_n are cutoff when the opposing lake breeze propagates into the averaging area.

2) 15 AUGUST

As in the July case, both u_n and C are generally larger for the Lake Erie breeze (Figs. 17b,d). These differences stem primarily from ΔT, which is 50%–100% larger for the Lake Erie breeze than for the Lake Ontario breeze (Fig. 18b). The weakness of the ambient flow (Fig. 18d) limits the differences in u_n and C between the two breezes, such that the inland propagation speed of the Lake Ontario breeze temporarily matches that of Lake Erie at 1530 EDT. After LBF collision, the merged boundary propagates slowly southward toward Lake Erie.

Compared to the July case, the magnitudes of u_n and C of the two lake breezes are broadly similar. However, in contrast to that case, w_{LBF} is slightly stronger for the Lake Erie LBF than that for Lake Ontario LBF over the three hours prior to their collision (Fig. 17f). These differences are maximized during the initiation of the Lake Ontario lake breeze over 1300–1400 EDT and gradually vanish. The weak ambient flow likely does not explain any differences in frontogenesis, and hence w_{LBF}, between the two LBFs. Rather, the stronger baroclinicity of the Lake Erie LBF is a more likely culprit. At the time of LBF collision (1600 EDT), the updraft along the merged boundary reaches nearly 0.5 m s^{-1}, exceeding that in the 18 July case by ~70%.

The enhanced subcloud ascent near the time of LBF collision could be either a cause or an effect of the enhanced moist convection in this case. Stronger subcloud updrafts tend to invigorate cloud-layer convection (e.g., Kirshbaum and Grant 2012), but these updrafts may also be enhanced by convection in the overlying layer (e.g., Wang and Kirshbaum 2015). To evaluate the feedbacks of cloud-layer latent heat release on the subcloud updraft, we restart the simulations of both the 18 July and 15 August cases around 2 h prior to LBF collision (1200 EDT and 1400 EDT, respectively) with cloud latent heating switched off. This timing limits divergence of these simulations from the original simulations prior to LBF collision. As shown in Figs. 17e and 17f, the elimination of latent heat feedbacks removes most of the differences in w_{LBF} between the two cases. Thus, the stronger subcloud updraft in the 15 August case is mostly an effect, rather than a cause, of enhanced moist convection in the cloud layer.

7. Conclusions

This study has used observations from the 2015 Environment and Climate Change Canada Pan/Parapan American Science Showcase (ECPASS) and real-case, cloud-resolving numerical simulations with the WRF Model to investigate two cases of moist convection forced by lake-breeze convergence over southern Ontario (18 July and 15 August 2015). The target area was the Niagara Peninsula, where lake breezes from Lake Erie (to the south) and Lake Ontario (to the north) often collide during the afternoon. Both events were characterized by nominally high-surface-pressure conditions, with impinging upper-level ridges forcing large-scale descent. The absence of nearby organized precipitating systems facilitated isolation of the lake-breeze dynamics and its role in convection initiation.

Despite similar morning thermodynamic soundings and late-afternoon moist instabilities (CAPE $\sim$1000 J kg^{-1}), the observed midafternoon cumulus convection differed substantially between the two cases. Lake-breeze-forced cumuli in the first case were much shallower (cloud tops $\leq$6 km) and weaker (maximum reflectivity of 35 dBZ) than those in the second case ($>$8 km and 50 dBZ). The objectives herein were to characterize the processes leading to convective initiation in the two cases and to interpret what physical processes led to such differences in cumulus development.

Although the numerical simulations did not perfectly reproduce either event, they succeeded in capturing the substantial differences in cloud-top height and maximum radar reflectivity between the two cases. Thus, in conjunction with ECPASS observations, they provide a useful framework for addressing the above objectives. Based on a synthesis of the observations and simulations, the following conclusions are reached:

1) The moderate southwesterly ambient winds in the 18 July case caused the Lake Erie breeze to propagate much faster inland than the Lake Ontario breeze, the latter of which was held fixed to the shoreline. By contrast, the light and variable ambient winds in the 15 August case led to a more symmetric lake-breeze inland propagation. These findings are consistent with previous studies showing that the lake-breeze inland propagation is enhanced by background tailwinds and suppressed by background headwinds (e.g., Sills et al. 2011).
2) Despite differences in lake-breeze timing and propagation between the two cases, the subcloud forcing for convection along the LBFs before their collision was similar. Consistent with Crook (1997) and previous work on southwestern Ontario lake breezes (e.g., King 1996; Sills 1998), the collision between Lakes Ontario and Erie LBFs over the Niagara Peninsula, and the attendant enhancement of subcloud ascent, led to the formation and/or intensification of convective precipitation. Although a spike in subcloud vertical motion near the time of lake-breeze frontal collision was simulated in the 15 August case, this enhancement stemmed from the positive feedback of latent heat release within the cloud layer. Excluding this effect, the subcloud forcing was found to be similar between the cases even after the LBF collision.
3) The principal mechanism behind the different cloud development in the two cases was differences in synoptic-scale midlevel warming over the course of the afternoon. The former case exhibited a large ($\sim$5 K) warming over the 850–650-hPa layer due to a combination of warm advection and large-scale descent, which created an afternoon inversion layer that inhibited convection. Although large-scale descent also occurred in the latter case, it was weaker and located farther aloft (750–350 hPa), and thus less effective at suppressing midlevel cumuli.

Although the convection was not particularly deep or severe in either case, the findings herein highlight the importance of subtle differences in transient large-scale forcing for regulating lake-breeze-forced convection, even under high pressure conditions. Given that current NWP grid spacings of O (1) km still cannot properly resolve mesoscale convergence lines responsible for initiating moist convection (Warren et al. 2014; Rousseau-Rizzi et al. 2017), these models cannot be expected to reliably predict lake-breeze-forced convection. Thus, studies like this one may provide added value to operational forecasting in regions susceptible to such convection.

Acknowledgments. The authors acknowledge funding from the Natural Science and Engineering Research Council (NSERC) Grant NSERC/RGPIN 418372-17. Numerical simulations were performed on the Guillimin supercomputer at McGill University, under the auspices of Calcul Québec and Compute Canada. Comments from three anonymous reviewers helped to improve the manuscript. The authors also thank Brian Greaves for technical assistance with the Aurora workstation used for lake-breeze front analysis.

REFERENCES

Al-Lami, A. M., A. M. Al-Salihi, and Y. K. Al-Timimi, 2017: Parameterization of the downward long wave radiation under clear-sky condition in Baghdad, Iraq. *Asian J. Appl. Sci.*, **10**, 10–17, https://doi.org/10.3923/ajaps.2017.10.17.

Alexander, L. S., 2012: Mesoscale boundaries and storm development in southwestern Ontario during ELBOW 2001. Ph.D. thesis, York University, Toronto, ON, Canada, 303 pp.

——, D. M. L. Sills, and P. A. Taylor, 2018: Initiation of convective storms at low-level mesoscale boundaries in southwestern Ontario. *Wea. Forecasting*, **33**, 583–598, https://doi.org/10.1175/WAF-D-17-0086.1.

Arritt, R. W., 1993: Effects of the large-scale flow on characteristic features of the sea breeze. *J. Appl. Meteor.*, **32**, 116–125, https://doi.org/10.1175/1520-0450(1993)032<0116:EOTLSF>2.0.CO;2.

Atkins, N. T., and R. M. Wakimoto, 1997: Influence of the synoptic-scale flow on sea breezes observed during CaPE. *Mon. Wea. Rev.*, **125**, 2112–2130, https://doi.org/10.1175/1520-0493(1997)125<2112:IOTSSF>2.0.CO;2.

Boodoo, S., D. Hudak, N. Donaldson, and M. Leduc, 2010: Application of dual-polarization radar melting-layer detection algorithm. *J. Appl. Meteor. Climatol.*, **49**, 1779–1793, https://doi.org/10.1175/2010JAMC2421.1.

Brook, J. R., P. A. Makar, D. M. L. Sills, L. Hayden, and R. McLaren, 2013: Exploring the nature of air quality over southwestern Ontario: Main findings from the Border Air Quality and Meteorology Study. *Atmos. Chem. Phys.*, **13**, 10 461–10 482, https://doi.org/10.5194/acp-13-10461-2013.

Bryan, G. H., J. C. Wyngaard, and J. M. Fritsch, 2003: Resolution requirements for the simulation of deep moist convection. *Mon. Wea. Rev.*, **131**, 2394–2416, https://doi.org/10.1175/1520-0493(2003)131<2394:RRFTSO>2.0.CO;2.

Carbone, R. E., J. W. Conway, N. A. Crook, and M. W. Moncrieff, 1990: The generation and propagation of a nocturnal squall line. Part I: Observations and implications for mesoscale predictability. *Mon. Wea. Rev.*, **118**, 26–49, https://doi.org/10.1175/1520-0493(1990)118<0026:TGAPOA>2.0.CO;2.

——, J. W. Wilson, T. D. Keenan, and J. M. Hacker, 2000: Tropical island convection in the absence of significant topography. Part I: Life cycle of diurnally forced convection. *Mon. Wea. Rev.*, **128**, 3459–3480, https://doi.org/10.1175/1520-0493(2000)128<3459:TICITA>2.0.CO;2.

Chiba, O., 1993: The turbulent characteristics in the lowest part of the sea breeze front in the atmospheric surface layer. *Bound.-Layer Meteor.*, **65**, 181–195, https://doi.org/10.1007/BF00708823.

Comer, N. T., and I. G. McKendry, 1993: Observation and numerical modelling of Lake Ontario breezes. *Appl. Opt.*, **31**, 481–499, https://doi.org/10.1080/07055900.1993.9649482.

Crook, N. A., 1997: Simulation of convective storms over the Tiwi Islands and comparison with observations from MCTEX. *Ninth Annual BMRC Modelling Workshop*, P. J. Meighen and J. D. Jasper, Eds., Bureau of Meteorology Rep., Vol. 64, 7–10.

Dehghan, A., Z. Mariani, S. Leroyer, P. Joe, D. Sills, and S. Bélair, 2018: Evaluation of modeled lake breezes using an enhanced observational network in southern Ontario: Case studies. *J. Appl. Meteor. Climatol.*, **57**, 1511–1534, https://doi.org/10.1175/JAMC-D-17-0231.1.

Derbyshire, S. H., I. Beau, P. Bechtold, J.-Y. Grandpeix, J.-M. Piriou, J.-L. Redelsperger, and P. M. M. Soares, 2004: Sensitivity of moist convection to environmental humidity. *Quart. J. Roy. Meteor. Soc.*, **130**, 3055–3079, https://doi.org/10.1256/qj.03.130.

Estoque, M. A., and J. M. Gross, 1981: Further studies of a lake breeze Part II: Theoretical study. *Mon. Wea. Rev.*, **109**, 619–634, https://doi.org/10.1175/1520-0493(1981)109<0619:FSOALB>2.0.CO;2.

——, and H. W. Lai, 1976: A lake breeze over southern Lake Ontario. *Mon. Wea. Rev.*, **104**, 386–396, https://doi.org/10.1175/1520-0493(1976)104<0386:ALBOSL>2.0.CO;2.

Fabry, F., 2015: *Radar Meteorology: Principles and Practice*. Cambridge University Press, 272 pp.

Greaves, B., R. Trafford, N. Driedger, R. Paterson, D. Sills, D. Hudak, and N. Donaldson, 2001: The AURORA nowcasting platform—Extending the concept of a modifiable database for short range forecasting. Preprints, *17th Int. Conf. on Interactive Information and Processing Systems for Meteorology, Oceanography, and Hydrology*, Albuquerque, NM, Amer. Meteor. Soc., 236–239.

Hayden, K. L., and Coauthors, 2011: Aircraft study of the impact of lake-breeze circulations on trace gases and particles during BAQS-Met 2007. *Atmos. Chem. Phys.*, **11**, 11 497–11 546, https://doi.org/10.5194/acpd-11-11497-2011.

Hudak, D., P. Rodriguez, G. Lee, A. Ryzhkov, F. Fabry, and N. Donaldson, 2006: Winter precipitation studies with a dual polarized C-band radar. Preprints, *Fourth European Conf. on Radar in Meteorology and Hydrology (ERAD 2006)*, Barcelona, Spain, Servei Meteorologic de Catalunya, 9–12.

Joe, P., and Coauthors, 2018: The Environment Canada Pan and Parapan American Science Showcase project. *Bull. Amer. Meteor. Soc.*, **99**, 921–953, https://doi.org/10.1175/BAMS-D-16-0162.1.

Keen, C. S., and W. A. Lyons, 1978: Lake/land breeze circulations on the western shore of Lake Michigan. *J. Appl. Meteor.*, **17**, 1843–1855, https://doi.org/10.1175/1520-0450(1978)017<1843:LBCOTW>2.0.CO;2.

King, P., 1996: A long-lasting squall line induced by interacting lake breezes. Preprints, *18th Conf. on Severe Local Storms*, San Francisco, CA, Amer. Meteor. Soc., 764–767.

——, and Coauthors, 1999: ELBOW: An experiment to study the effects of lake breezes on weather in southern Ontario. *CMOS Bull.*, **27**, 35–41.

King, P. W. S., M. J. Leduc, D. M. L. Sills, N. R. Donaldson, D. R. Hudak, P. Joe, and B. P. Murphy, 2003: Lake breezes in southern Ontario and their relation to tornado climatology. *Wea. Forecasting*, **18**, 795–807, https://doi.org/10.1175/1520-0434(2003)018<0795:LBISOA>2.0.CO;2.

Kirshbaum, D. J., and A. L. M. Grant, 2012: Invigoration of cumulus cloud fields by mesoscale ascent. *Quart. J. Roy. Meteor. Soc.*, **138**, 2136–2150, https://doi.org/10.1002/qj.1954.

Kristovich, D. A. R., and Coauthors, 2017: The Ontario Winter Lake-effect Systems field campaign: Scientific and educational adventures to further our knowledge and prediction of lake-effect storms. *Bull. Amer. Meteor. Soc.*, **98**, 315–332, https://doi.org/10.1175/BAMS-D-15-00034.1.

Leduc, M. J., B. Murphy, and P. Joe, 1993: The structure and evolution of the 28 August 1990 tornado-producing supercell in southwestern Ontario. Preprints, *17th Conf. on Severe Local Storms*, St. Louis, MO, Amer. Meteor. Soc., 164–167.

Leroyer, S., S. Bélair, S. Z. Husain, and J. Mailhot, 2014: Subkilometer numerical weather prediction in an urban coastal area: A case study over the Vancouver Metropolitan Area. *J. Appl. Meteor. Climatol.*, **53**, 1433–1453, https://doi.org/10.1175/JAMC-D-13-0202.1.

Levy, I., and Coauthors, 2010: Unraveling the complex local-scale flows influencing ozone patterns in the southern Great Lakes of North America. *Atmos. Chem. Phys.*, **10**, 10 895–10 915, https://doi.org/10.5194/acp-10-10895-2010.

Lyons, W. A., 1972: The climatology and prediction of the Chicago lake-breeze. *J. Appl. Meteor.*, **11**, 1259–1270, https://doi.org/10.1175/1520-0450(1972)011<1259:TCAPOT>2.0.CO;2.

——, and H. S. Cole, 1973: Fumigation and plume trapping on the shores of Lake Michigan during stable onshore flow. *J. Appl. Meteor.*, **12**, 494–510, https://doi.org/10.1175/1520-0450(1973)012<0494:FAPTOT>2.0.CO;2.

Mahoney, W. P., 1988: Gust front characteristics and the kinematics associated with interacting thunderstorm outflows. *Mon. Wea. Rev.*, **116**, 1474–1491, https://doi.org/10.1175/1520-0493(1988)116<1474:GFCATK>2.0.CO;2.

Makar, P. A., and Coauthors, 2010: Mass tracking for chemical analysis: The causes of ozone formation in southern Ontario during BAQS-Met 2007. *Atmos. Chem. Phys.*, **10**, 11 151–11 173, https://doi.org/10.5194/acp-10-11151-2010.

Mariani, Z., A. Dehghan, P. Joe, and D. Sills, 2018: Observations of lake-breeze events during the Toronto 2015 Pan-American Games. *Bound.-Layer Meteor.*, **166**, 113–135, https://doi.org/10.1007/s10546-017-0289-3.

McCaul, E. W., and M. L. Weisman, 2001: The sensitivity of simulated supercell structure and intensity to variations in the shapes of environmental buoyancy and shear profiles. *Mon. Wea. Rev.*, **129**, 664–687, https://doi.org/10.1175/1520-0493(2001)129<0664:TSOSSS>2.0.CO;2.

McKendry, I., and N. Roulet, 1994: Sea breezes and advective effects in southwest James Bay. *J. Geophys. Res.*, **99**, 1623–1634, https://doi.org/10.1029/92JD02286.

Moroz, W. J., 1967: A lake breeze on the eastern shore of Lake Michigan: Observation and model. *J. Atmos. Sci.*, **24**, 337–355, https://doi.org/10.1175/1520-0469(1967)024<0337:ALBOTE>2.0.CO;2.

Niziol, T. A., 1987: Operational forecasting of lake effect snowfall in western and central New York. *Wea. Forecasting*, **2**, 310–321, https://doi.org/10.1175/1520-0434(1987)002<0310:OFOLES>2.0.CO;2.

Peace, R. L., and R. B. Sykes, 1966: Mesoscale study of a lake effect snow storm. *Mon. Wea. Rev.*, **94**, 495–507, https://doi.org/10.1175/1520-0493(1966)094<0495:MSOALE>2.3.CO;2.

Purdom, J. F. W., 1976: Some uses of high-resolution GOES imagery in the mesoscale forecasting of convection and its behavior. *Mon. Wea. Rev.*, **104**, 1474–1483, https://doi.org/10.1175/1520-0493(1976)104<1474:SUOHRG>2.0.CO;2.

Reinking, R. F., and Coauthors, 1993: The Lake Ontario Winter Storms (LOWS) Project. *Bull. Amer. Meteor. Soc.*, **74**, 1828–1850, https://doi.org/10.1175/1520-0477-74-10-1828.

Rotunno, R., J. B. Klemp, and M. L. Weisman, 1988: A theory for strong, long-lived squall lines. *J. Atmos. Sci.*, **45**, 463–485, https://doi.org/10.1175/1520-0469(1988)045<0463:ATFSLL>2.0.CO;2.

Rousseau-Rizzi, R., D. J. Kirshbaum, and M. K. Yau, 2017: Initiation of deep convection over an idealized mesoscale convergence line. *J. Atmos. Sci.*, **74**, 835–853, https://doi.org/10.1175/JAS-D-16-0221.1.

Samiro, K. P., 2015: *High-Resolution Analysis of the Initiation of Deep Convection Forced by Boundary-Layer Processes*. KIT Scientific Publishing, 228 pp.

Segal, M., R. W. Arritt, J. Shen, C. Anderson, and M. Leuthold, 1997: On the clearing of cumulus clouds downwind from lakes. *Mon. Wea. Rev.*, **125**, 639–646, https://doi.org/10.1175/1520-0493(1997)125<0639:OTCOCC>2.0.CO;2.

Shenfeld, L., and F. D. Thompson, 1962: The thunderstorm of August 9, 1961 at Hamilton, Ontario, Canada. Canada Meteorological Branch, 24 pp.

Sills, D. M. L., 1998: Lake and land breezes in southwestern Ontario: Observation, analyses, and numerical modelling. Ph.D. thesis, York University, 361 pp.

——, and J. R. Salmon, 1994: Southern Ontario oxidant study—Meteorological measurements. Final data report, York University and Zephyr North, 87 pp. [Available from Prof. P. Taylor, Department of Earth and Atmospheric Sciences, York University, 4700 Keele St., North York, ON M3J 1P3, Canada.]

——, P. Taylor, P. King, W. Hocking, and I. Nichols, 2002: ELBOW 2001studying the relationship between lake breezes and severe weather: Project overview and preliminary results. Preprints, *21st Severe Local Storms Conf.*, San Antonio, TX, Amer. Meteor. Soc., 611–614.

——, J. R. Brook, I. Levy, P. A. Makar, J. Zhang, and P. A. Taylor, 2011: Lake breezes in the southern Great Lakes region and their influence during BAQS-Met 2007. *Atmos. Chem. Phys.*, **11**, 7955–7973, https://doi.org/10.5194/acp-11-7955-2011.

Skamarock, W. C., and Coauthors, 2008: description of the Advanced Research WRF version 3. NCAR Tech. Note NCAR/TN-475+STR, 113 pp., https://doi.org/10.5065/D68S4MVH.

Steyn, D. G., 2003: Scaling the vertical structure of sea breezes revisited. *Bound.-Layer Meteor.*, **107**, 177–188, https://doi.org/10.1023/A:1021568117280.

Thiébaux, J., E. Rogers, W. Wang, and B. Katz, 2003: A new high-resolution blended real-time global sea surface temperature analysis. *Bull. Amer. Meteor. Soc.*, **84**, 645–656, https://doi.org/10.1175/BAMS-84-5-645.

Wang, C.-C., and D. J. Kirshbaum, 2015: Thermally forced convection over a mountainous tropical island. *J. Atmos. Sci.*, **72**, 2484–2506, https://doi.org/10.1175/JAS-D-14-0325.1.

Warren, R. A., D. J. Kirshbaum, R. S. Plant, and H. W. Lean, 2014: A 'Boscastle-type' quasi-stationary convective system over the UK southwest peninsula. *Quart. J. Roy. Meteor. Soc.*, **140**, 240–257, https://doi.org/10.1002/qj.2124.

Wentworth, G. R., J. G. Murphy, and D. M. L. Sills, 2015: Impact of lake breezes on ozone and nitrogen oxides in Greater Toronto Area. *Atmos. Environ.*, **109**, 52–60, https://doi.org/10.1016/j.atmosenv.2015.03.002.

Wilks, D. S., 2011: *Statistical Methods in the Atmospheric Sciences*. 3rd ed. International Geophysics Series, Vol. 100, Academic Press, 704 pp.

Wilson, J. W., and W. E. Schreiber, 1986: Initiation of convective storms by radar-observed boundary layer convergent lines. *Mon. Wea. Rev.*, **114**, 2516–2536, https://doi.org/10.1175/1520-0493(1986)114<2516:IOCSAR>2.0.CO;2.

——, T. M. Weckwerth, J. Vivekanandan, R. M. Wakimoto, and R. W. Russell, 1994: Boundary layer clear-air radar: Origin of echoes and accuracy of derived winds. *J. Atmos. Oceanic Technol.*, **11**, 1184–1206, https://doi.org/10.1175/1520-0426(1994)011<1184:BLCARE>2.0.CO;2.

Wood, R., I. M. Stromberg, and P. R. Jonas, 1999: Aircraft observations of sea-breeze frontal structure. *Quart. J. Roy. Meteor. Soc.*, **125**, 1959–1995, https://doi.org/10.1002/qj.49712555804.